

Episodic Star Formation - I. Overview and Scatter of the Star-Forming Main Sequence

YUQIAN GUI¹,¹ DANDAN XU,¹ HAOYI WANG,¹ XUELUN MEI,¹ ENCI WANG,² CHENG LI,¹ AND STIJN WUYTS³

¹*Department of Astronomy, Tsinghua University, Beijing 100084, China*

²*School of Astronomy and Space Sciences, University of Science and Technology of China, Hefei, Anhui, 230026, China*

³*Department of Physics, University of Bath, Claverton Down, Bath BA2 7AY, UK*

ABSTRACT

Episodic star formation cycles in both high- and low-redshift galaxies have gained more and more evidence. This paper aims to understand the detailed physical processes behind such behaviors and investigate how such an episodic star-forming scenario can explain the scatter in star-formation rate (SFR) of star-forming main-sequence galaxies. This is achieved through tracing back in time the history of $z = 0$ star-forming central galaxies in the TNG100 simulation over the past 7 – 8 Gyrs. As the first paper in this series, we provide an overview of the episodic star formation history. We find that two branches of star formation typically develop during each episode: while one branch happens in heavily metal-enriched gas in the centers of galaxies, a secondary branch starts in lower-metallicity regions at galaxy outskirts where fresh gas first arrives, and gradually progresses to inner regions of galaxies. Additionally, the temporal variation in the SFR at galaxy outskirts is more significant than that at centers. As a consequence, the metallicities in both gas and young stars exhibit remarkably different distributions between SFR peaks and valleys. The resulting temporal SFR fluctuation within individual galaxies has an average of ~ 0.2 dex, while the intrinsic differentiation between (the historical mean of) galaxies is ~ 0.15 dex. These two together can well account for the scatter in SFR of ~ 0.25 dex as observed for $z = 0$ star-forming main-sequence galaxies.

Keywords: Galaxy physics (612) — Galaxy properties (615) — Galaxy stellar content (621) — Galaxy processes (614) — Galaxy evolution (594) — Galaxy chemical evolution (580)

1. INTRODUCTION

The star formation history (SFH) of galaxies has always been among the most heated topics in the field of galaxy evolution. Observationally, the discoveries of galaxy bimodalities in color, morphology, and stellar kinematics (e.g., Tully et al. 1982; Strateva et al. 2001; Hogg et al. 2003; Budavári et al. 2003; Bell et al. 2004; Balogh et al. 2004; Baldry et al. 2004; Morselli et al. 2017; Wang et al. 2020, 2025) have generally revealed two distinct populations of galaxies in the present-day Universe, one on the so-called ‘star formation main sequence’ (SFMS, e.g., Brinchmann et al. 2004; Salim et al. 2007; Noeske et al. 2007a; Daddi et al. 2007; Elbaz et al. 2007; Whitaker et al. 2012a; Speagle et al. 2014a; Pannella et al. 2015; Pearson et al. 2018; Leslie et al. 2020; Popesso et al. 2023), also referred to as the ‘blue cloud’; and one with significantly lower or already ceased star formation activity, also dubbed the ‘red sequence’ (e.g., Kauffmann et al. 2003; Faber et al. 2007; Schaye et al. 2010; Peng et al. 2010, 2015; Rodighiero et al. 2011;

Renzini 2016; Tacchella et al. 2022). A classical picture for the formation path of the former suggests generally mild star-formation rate (SFR) variations throughout their evolutionary history as they ride along the SFMS until today. The latter population, on the other hand, underwent a transition from the SFMS at high redshift to a more quiescent or completely quenched status by the present day. This study focuses on the recent evolutionary history of the former class since $z \sim 1$, in particular from perspectives regarding how galaxies move up and down the SFMS, the origin of its dispersion, and the properties of galaxies above and below the SFMS, which remain not fully understood.

The overall cosmic star formation rate density peaks around $z \sim 2$ and has been declining ever since (Madau & Dickinson 2014). The specific star formation rate (sSFR) of SFMS galaxies also decreases strongly towards lower redshift as a consequence of a decreasing cosmological gas accretion rate (e.g., Dutton et al. 2010; Tacchella et al. 2013; Dekel et al. 2013; Lilly et al. 2013; Forbes et al. 2014; Schreiber et al. 2015). It has been

observed that the SFMS has a typical scatter of 0.2-0.3 dex across a wide range of redshifts (e.g., Noeske et al. 2007b; Whitaker et al. 2012b; Speagle et al. 2014b; Pearson et al. 2018). The finite scatter in star-formation activity at fixed stellar mass is attributed to both internal and external factors. On the one hand, supernovae and stellar wind feedback (e.g., Dekel & Silk 1986; Murray et al. 2005; Ceverino & Klypin 2009; Hopkins et al. 2014a, 2023; El-Badry et al. 2016; Hayward & Hopkins 2017; Shin et al. 2023; Dome et al. 2025) as well as supermassive black hole feedback (e.g., Di Matteo et al. 2005; Springel et al. 2005; Croton et al. 2006; Ciotti & Ostriker 2007; Cattaneo et al. 2009; Fabian 2012; Cicone et al. 2014, 2016) may affect both the thermal and kinematic state of the interstellar medium (ISM) or even the circumgalactic medium (CGM), and thus regulate the rate of star formation. On the other hand, galaxy interaction and merger activities may affect cold gas accretion rates and thus modulate galaxy SFRs (e.g., Barnes & Hernquist 1991; Mihos & Hernquist 1996; Conselice et al. 2003; Hopkins et al. 2006; Cox et al. 2006; Smethurst et al. 2015; Wang et al. 2022). As a consequence, the SFR of individual galaxies can fluctuate on both short and long timescales, in particular among low-mass or high- z galaxies, resulting in the observed scatter around the SFMS (White & Rees 1978; Dutton et al. 2010; Dekel & Burkert 2014; Somerville & Davé 2015; Sparre et al. 2017; Orr et al. 2017; Feldmann et al. 2017; Tacchella et al. 2018; Behroozi et al. 2019; Caplar & Tacchella 2019; Iyer et al. 2020; Wan et al. 2024; Mintz et al. 2025; McClymont et al. 2025).

In the high- z Universe ($z > 1 - 2$), the fluctuation in SFR is also highly relevant in explaining the discovery of overabundant UV-bright galaxies as recently revealed by JWST (Donnan et al. 2023, 2024; Endsley et al. 2024b; Leethochawalit et al. 2023; Pérez-González et al. 2023; Robertson et al. 2024; Whitler et al. 2025). This is because a bursty/fluctuating SFH with a high variability in SFR may temporarily scatter high- z galaxies to large UV luminosities and thus explain such observations, along with the scatter of the SFMS (Anglés-Alcázar et al. 2017; Faucher-Giguère 2018; Tacchella et al. 2020; Shen et al. 2023; Sun et al. 2023; Mason et al. 2023; Kravtsov & Belokurov 2024; Endsley et al. 2024a; Ciesla et al. 2024; McClymont et al. 2025; Mintz et al. 2025).

Fluctuating/bursty SFHs can be considered one manifestation of episodic behavior in galaxy growth. High- z galaxies typically go through episodic cycles of gas compaction, depletion, and replenishment, and eventually cease their star formation and become quenched (e.g., Zolotov et al. 2015; Tacchella et al. 2016, 2020; Mc-

Clymont et al. 2025). It is worth noting that such a bursty/fluctuating SFH is not unique for high- z galaxies, and more and more evidences also suggest their universality among star-forming galaxies across all redshifts, in particular among lower mass galaxies (Tolstoy et al. 2009; McQuinn et al. 2010a,b; Weisz et al. 2011; Wang & Lilly 2020; Yin et al. 2023; Muñoz López et al. 2025; Perry et al. 2025; Wan et al. 2025). Unlike (the present-day *quiescent* descendants of) their high- z counterparts, these galaxies have nearly always maintained their star-formation rates to a certain level and never evolved to a long-term quenched status, and therefore remain star-forming to the present day.

In this regard, a number of theoretical studies have conducted relevant investigations (e.g., Lilly et al. 2013; Wang et al. 2019; Wang & Lilly 2021, 2022a,b). Based on the variation of star formation across the population of the MaNGA sample, Wang et al. (2019) proposed that the scatter of the SFMS can be understood by the time-varying gas inflow rate. This scenario predicts that the scatter of galaxies on the SFMS strongly depends on galaxy size, with smaller sizes for larger scatter. Interestingly, this is seen in observations across different datasets and redshifts (Wuyts et al. 2011; Wang et al. 2018).

Such a fluctuating SFH in lower- z star-forming galaxies has also been found in many of the latest cosmological hydrodynamical simulations. For example, utilizing the FIRE simulation (Hopkins et al. 2014b, 2018; Feldmann et al. 2023), Cenci et al. (2024) investigated the ‘breathing mode’ of galaxy starbursts, on long and short timescales. With the Magneticum Pathfinder simulation (Hirschmann et al. 2014), Fortuné et al. (2025) revealed cycles of quenching and rejuvenation on timescales of ~ 1 Gyr for a large fraction of $z = 0$ SFMS galaxies. Wang et al. (2022) also demonstrated a clear episodic SFH of present-day star-forming disc galaxies using the TNG100 simulation (Springel et al. 2018; Nelson et al. 2018; Naiman et al. 2018; Marinacci et al. 2018; Pillepich et al. 2018a). In this particular study, the authors presented how the CGM of (central) galaxies acquires a supply of cold gas ($T < 2 \times 10^4$ K) and inherits angular momentum as a consequence of galaxy mergers and interactions at ~ 100 kpc scales. At the same time, the CGM also receives thermal and kinetic modulation of internal feedback processes out to several tens of kiloparsecs. The combined effect regulates the replenishment and depletion of the cold gas reservoir in a rhythmic fashion, leading to a pulsating motion of the cold circumgalactic gas highly synchronized with an episodic SFH of the galaxy.

This paper series is a follow-up of Wang et al. (2022), conducting a detailed investigation to better understand the episodic star formation behavior of present-day SFMS galaxies and how such a behavior may explain some of the observed relations. This is achieved through tracing back in time the history of star-forming galaxies at $z = 0$ in the TNG100 simulation and investigating the co-evolution of various galaxy properties as galaxies go through SFR peaks and troughs in their history since $z \sim 1$. In this first paper of the series, we present an overview and the timeline of the episodic SFH of $z = 0$ SFMS galaxies. In particular, we show that major differences exist among galaxy properties between SFR peaks and valleys, and that the resulting temporal SFR fluctuation within individual galaxies (~ 0.2 dex) together with intrinsic scatter among different galaxies (~ 0.15 dex) can account for the scatter of the SFMS today (~ 0.25 dex). In the second paper of this series (Mei et al. in prep), we will show that the simulation successfully reproduces the observed anti-correlation between SFR and metallicity, and suggest that the episodic SFH can also offer a plausible explanation to the observed fundamental metallicity relation (Mannucci et al. 2010). In the third paper of this series (Wang et al. in prep), we further present the key role that the cold gas plays under the combined internal and external modulation across a wide range of scales in such an episodic formation scenario.

The paper is organized as follows: In Section 2, we introduce the details of the simulation, galaxy sample selection, and galaxy properties investigated in this study. In Section 3, we present the overview of episodic SFH by investigating the evolution of gas and stellar mass, metallicity, as well as their spatial distributions. We will show that two star-formation branches of distinct chemical signatures exist during each episode, and the metallicities in both gas and young stars exhibit remarkably different distributions between SFR peaks and valleys. In Section 4, we present the degree to which the temporal fluctuation in SFR can account for the scatter of SFMS. The conclusions and some further discussions are given in Section 5. Throughout the paper, we adopt the same cosmology as used in the IllustrisTNG simulation, which is based on the Planck results (Planck Collaboration et al. 2016), i.e., a total matter density of $\Omega_m = 0.3089$, a baryonic matter density of $\Omega_b = 0.0486$, and a Hubble constant $h = H_0/(100 \text{ kms}^{-1} \text{ Mpc}^{-1}) = 0.6774$, assuming a flat Λ CDM universe.

2. METHODOLOGY

2.1. The simulation

The *Next Generation Illustris Simulations* (IllustrisTNG, TNG hereafter; Springel et al. 2018; Nelson et al. 2018, 2019a; Naiman et al. 2018; Marinacci et al. 2018; Pillepich et al. 2018a, 2019) are a set of state-of-the-art magneto-hydrodynamic cosmological simulations using the moving-mesh code AREPO (Springel 2010) for galaxy formation and evolution. The simulation, compared to previous galaxy formation cosmological simulations, has implemented various modifications to galactic wind feedback, stellar evolution, and chemical enrichment (Pillepich et al. 2018b). In this study, we use one of the TNG versions with a cubic box of 110.7 Mpc side length (TNG100 hereafter), which was run with a gravitational softening length of $0.5 h^{-1} \text{ kpc}$ and mass resolution of $1.4 \times 10^6 M_\odot$ and $7.5 \times 10^6 M_\odot$ for the baryonic and dark matter, respectively. In TNG100, the SUBFIND algorithm (Springel et al. 2001; Dolag et al. 2009) is used to identify host dark matter halos. General galaxy properties were calculated and publicly released by the TNG collaboration¹ (Nelson et al. 2019b).

2.2. Sample selection: evaluating scatter in SFMS

One goal of this study is to demonstrate to what extent the $z = 0$ SFMS scatter can be accounted for by the temporal fluctuation in SFR within individual star-forming galaxies according to the TNG100 simulation. To first form our SFMS sample, we take all star-forming central galaxies with stellar mass $M_* \geq 10^{9.5} M_\odot$ at $z = 0$ from the simulation, explicitly avoiding all satellites whose SFH may be affected by their host group or cluster environment (Peng et al. 2010; Bahé & McCarthy 2015). Here ‘star-forming’ (SF) is defined as the logarithmic specific SFR $\log [\text{sSFR}/\text{Gyr}^{-1}] \geq -1.5$, which is approximately 0.5 dex below the mean sSFR of galaxies with $M_* < 3 \times 10^{10} M_\odot$ at $z = 0$ (for more details, see Lu et al. 2021, 2022). Under this definition, our SFMS sample contains 5051 galaxies.

We further trace the merger history of these galaxies and specifically consider the main progenitor branch up to $z = 1$ (snapshot 050). At each redshift, we determine the ridge of SFMS using a linear regression fitted to the $\log \text{SFR} - \log M_*$ distribution of the collection of the corresponding galaxy progenitors. We then calculate for each galaxy the difference in the logarithmic SFR from the ridge at that redshift (i.e., the main-sequence offset), denoted as $\Delta \text{MS}(z)$. For the derived ΔMS among all sample galaxies at all redshifts, we capture the degree of main-sequence offset for each galaxy using two different statistics: (1) the present-

¹ <http://www.tng-project.org/data/>

day main-sequence offset ($\Delta MS_{z=0}$); and (2) the historically averaged main-sequence offset since $z = 1$ ($\text{avg}(\Delta MS)$), denoting in general whether a galaxy has primarily lived above/below the MS ridge, and by how much on average. In order to also capture the temporal SFR fluctuation within a given galaxy since $z = 1$, we fit a linear relation to the $\log \text{SFR} - \log(1+z)$ path of each galaxy. We then calculate, for a given galaxy, the scatter $\sigma_{\text{SFR,rel}}$ in logarithmic SFR relative to its long-term redshift evolution. Specifically, $\sigma_{\text{SFR,rel}} = \sqrt{\frac{1}{N} \sum [\log \text{SFR}(z) - \overline{\log \text{SFR}_{\text{lin}}}(z)]^2}$, where summation is carried out over all N snapshots since $z = 1$ and $\overline{\log \text{SFR}_{\text{lin}}}(z)$ is the long-term redshift-dependent value given by the linear fitting. For all three properties introduced above, we quantify their 16-50-84 percentiles over all galaxies in the SFMS sample. The results are presented in Section 4.

We note that the reason we only trace the main progenitor history back to $z = 1$ is that we have observed a relatively more stable SFH of present-day star-forming galaxies from $z \sim 1$ till today, i.e., in the past 7–8 Gyrs. This can be clearly seen in Figure 9 from Lu et al. (2022): below $z \sim 1$, galaxies have, in general, experienced much less frequent larger-ratio mergers than at higher redshifts. In this study, we take $z = 1$ as an upper limit for the redshift range.

2.3. A further refined sample for peak-valley statistics

In order to demonstrate typical episodic star formation behavior and conduct statistics at SFR peaks and valleys, we further select a refined sample from present-day star-forming rotating disc galaxies for which the peaks and valleys can be clearly identified. This refined sample is constructed based on the galaxies studied in Lu et al. (2021, 2022), where classical star-forming rotating disc galaxies were identified according to their specific star formation rates, bulge-to-total luminosity ratios, and circular orbit fractions. A random selection was carried out to reduce the sample to a reasonably sized sample (see reference above for details). This resulted in a lower-mass sample containing 165 central galaxies with $9.5 \leq \log M_*/M_\odot \leq 10.3$ and a more massive sample containing 120 central galaxies with $10.3 \leq \log M_*/M_\odot \leq 11.2$ at $z = 0$.

For these 285 present-day star-forming rotating disc galaxies, we carry out a closer inspection of the redshift evolution along their main progenitor branch. We downselect to those galaxies that have typical episodic star-formation behavior with clearly defined major peaks and valleys since $z = 1$. This is achieved based on $\Delta \log [\text{SFR}/M_\odot \text{Gyr}^{-1}]$ – the difference in SFR between the identified adjacent peak and valley in a given peak-

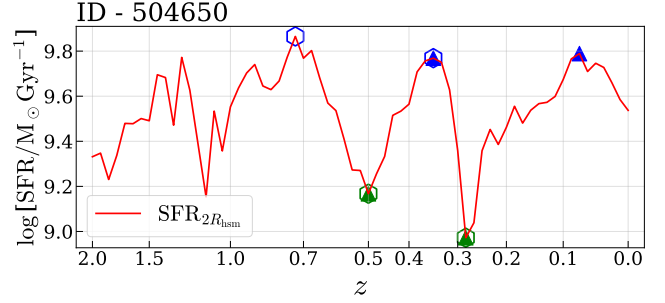


Figure 1. The star formation history of one of our sample galaxies (ID at $z = 0$ is 504650). The red line represents the SFR of this galaxy evaluated within $2R_{\text{hsm}}$. The green and blue upper triangles represent the valleys and peaks in the upward pairs. The blue and green hollow hexagons represent peaks and valleys in the downward pairs.

valley pair. For the SFH of each galaxy, we search for valley-to-peak (upward) pairs and peak-to-valley (downward) pairs which satisfy $\Delta \log [\text{SFR}/M_\odot \text{Gyr}^{-1}]$ greater than a given threshold and require that galaxies shall have at least two upward pairs or two downward pairs since $z \sim 1$, as an indication of at least two star-forming episodes (see Appendix A for a detailed description of the pair searching algorithm adopted).

For this study, we adopt 0.5 dex (in comparison to a ~ 0.25 dex scatter in the $z = 0$ SFMS) as the $\Delta \log [\text{SFR}/M_\odot \text{Gyr}^{-1}]$ threshold to downselect a refined galaxy sample to conduct the peak-valley statistics in order to gain insight into the typical galaxy conditions during these extreme moments. Among the total of 285 $z = 0$ star-forming rotating disc galaxies, 191 galaxies (103 in the lower mass range and 88 in the more massive range) have since $z \sim 1$ experienced at least two upward or two downward peak-valley pairs that satisfy $\Delta \log [\text{SFR}/M_\odot \text{Gyr}^{-1}] > 0.5$ dex (with a total of 363 upward pairs and 382 downward pairs). Fig. 1 shows the star formation history of an example galaxy (subfindID-504650 at $z = 0$), where the identified peaks and valleys are labeled by blue and green symbols, and the upward pairs and downward pairs are denoted by solid triangles and hollow hexagons, respectively.

We note that the quantitative results in the statistical comparisons in galaxy properties among SFR peaks and valleys, as well as the time signatures of the episodic evolution of the investigated properties would certainly depend on the adopted $\Delta \log [\text{SFR}/M_\odot \text{Gyr}^{-1}]$ threshold. For this reason, we have also tested five different thresholds, being 0.1, 0.2, 0.3, 0.4, and 0.5 dex, and investigated how the number of galaxies that satisfy such criteria and the timescales of identified peak-valley pairs would vary with the choice of the threshold. We present the results in Appendix B.

2.4. Galaxy properties studied

In this work, we investigate the evolution of several galaxy properties along with SFR, including $g-r$ color, half stellar-mass radius R_{hsm} , cold gas mass M_{cold} , stellar and gas-phase metallicity Z_* and Z_{gas} . In particular, the properties are usually measured within $2R_{\text{hsm}}$, which are referred to as global galactic quantities.

For the gas properties, we follow two components of cold gas. The first component is *non-SF* gas with an effective temperature $T < 2 \times 10^4$ K – a typical temperature below which atomic hydrogen can cool and thus is able to form stars (provided it reaches sufficient density) (Kereš et al. 2005; Dekel & Birnboim 2006; Dekel et al. 2009). Observationally, this gas can be traced by the Ly- α line (Katz & Gunn 1991; Fardal et al. 2001) and HI 21 cm emission (Draine 2011; Saintonge & Catinella 2022). This cold but *non-SF* gas sits at a density below the adopted star-forming threshold of $n_{\text{H}} \sim 0.1 \text{ cm}^{-3}$ (by the simulation), representing the radiatively cooled, dense gas in galaxies (Vogelsberger et al. 2012; Martizzi et al. 2019). We refer to this gas component as the ‘non-SF cold gas reservoir’. The second component is star-forming gas. This gas sits at a density above the star-forming threshold, and is numerically enforced with an effective equation of state which describes a two-phase medium composed of both hot and cold gas of the interstellar medium (Springel & Hernquist 2003). We refer to this gas as the ‘SF gas pool’. In this paper, we follow the evolution of the enclosed mass, surface density, and metallicity distribution of both types of cold gas components during the episodic SFH of galaxies.

2.5. Stacking galaxies for peak-valley statistics

In order to demonstrate the most significant features and differences between the peak and valley moments, we stack galaxy properties at the identified peaks and valleys of all 191 galaxies in the refined galaxy sample. In order to further extract the general statistical trends around peaks and valleys, we take the neighboring snapshots around these moments according to a given time offset. To reduce noise/fluctuation at shorter time scales, for any given galaxy property at a specific snapshot i , we first calculate the mean of this property among the three adjacent snapshots, i.e., $i-1$, i , and $i+1$. For any given time offset around peaks/valleys, the corresponding galaxy properties are then interpolated using the smoothed values at two adjacent snapshots. We line up the moments of all peaks/valleys and take the smoothed and interpolated values of a given galaxy property under investigation as its zero point. For any given time offset, we then calculate the difference in this property from the zero-point value. By doing so, the

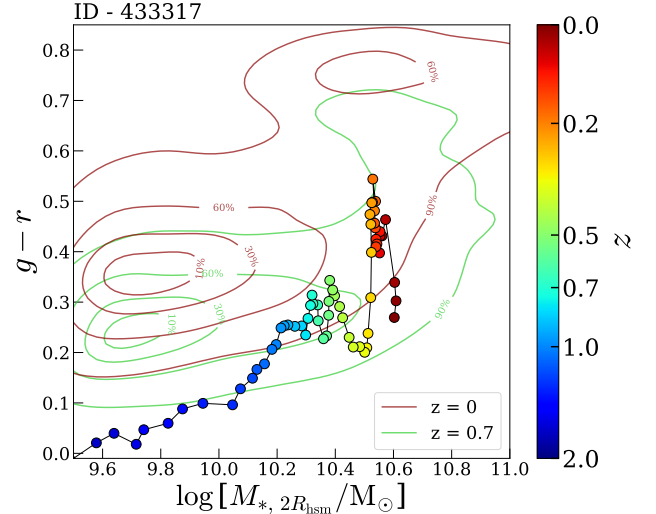


Figure 2. The $g-r$ color - $\log M_*$ evolutionary track for one example galaxy (ID-433317). The contours indicate the distribution of color as a function of stellar mass M_* of central galaxies in today’s universe (red contour) and at $z = 0.7$ (green contour), respectively. The black solid line marks the evolutionary track of the galaxy, with circles color-coded by redshifts.

galaxy-to-galaxy difference among the population can be markedly eliminated, only preserving the internal and temporal offsets relative to peaks and valleys for any given galaxy. Then we can investigate systematic differences between the peak and valley moments as well as the evolutionary trend of galaxy properties around these extrema.

3. RESULTS: OVERVIEW

In this section, we first present an overview of the episodic star formation scenario, including a detailed pattern regarding how the star formation zone propagates through a galaxy during each episode, as well as a detailed comparison of galaxy properties at SFR peaks and valleys. In Section 3.1 and 3.2, we first show how galaxy color and the cold gas content vary with time, respectively. In Section 3.3, we demonstrate the presence of two star-formation branches during each episode, and in Section 3.4, we show how they are intertwined with different radial distributions in metallicity of young stars and gas between SFR peak and valley moments.

3.1. Temporal variation of galaxy color variation

Galaxy color strongly correlates with the star formation activity. As the SFR rises and falls during the episodic evolution, the color also changes accordingly. Fig. 2 shows the evolutionary history of an example galaxy (ID-433317) in the color-mass diagram. The two contours in this figure indicate the distribution of $g-r$

color as a function of stellar mass M_* for all central galaxies at $z = 0$ (red contour) and at $z = 0.7$ (green contour). In each case, four contour lines indicate the regions that include 10%, 30%, 60%, and 90% of the total sample. The solid line indicates the evolutionary track of this galaxy, color-coded by redshift. It can be seen that the color of this galaxy has an overall trend of becoming redder, accompanied by multiple rapid variations due to changes in SFR, especially since $z \sim 1$.

It is worth noting that the $g - r$ color of this galaxy reaches its global peak at $z \approx 0.2$, when its SFR was 0.457 dex below the main sequence at that time. Compared to the overall color distribution at that time, this galaxy used to be much redder than its star-forming counterparts and could even be identified as a ‘green valley’ galaxy (Salim 2014; Mendez et al. 2011; Smith et al. 2022). However, soon after that, it rejuvenated and returned to the blue cloud once its star formation was ignited again. Among our present-day star-forming rotating disc sample of 285 galaxies, 37% have had their historical SFR 0.5 dex below the main sequence ridge (at the corresponding redshift) at least once since $z \sim 1$, and rejuvenated later to get back to the SFMS, or even above the ridge, at $z = 0$.

3.2. Temporal variation of the cold gas content

As was already investigated in Wang et al. (2022), the rise and fall of SFR react (with a time delay) to the change of the circumgalactic cold gas reservoir going out to ~ 100 kpc. To get an overview of this episodic behavior, we present the time evolution of the cold gas content and gas-phase metallicity along with SFR since $z \sim 2$ for an example galaxy (ID-601819) in Fig. 3. The top panel presents the temporal variation of $\text{SFR}_{\leq 2R_{\text{hsm}}}$ (global, in solid line) and $\text{SFR}_{\leq 0.5R_{\text{hsm}}}$ (central, in dashed line). The second panel presents the evolution of cold gas mass within $2R_{\text{hsm}}$ for the *star-forming* gas (M_{SF} , solid line) and the cold *non-SF* gas ($M_{\text{cold, non-SF}}$, dashed line). As can be seen, the evolution of M_{SF} traces that of $\text{SFR}_{\leq 2R_{\text{hsm}}}$ well, while the evolution of $\text{SFR}_{\leq 2R_{\text{hsm}}}$ is not fully synchronized with that of $M_{\text{cold, non-SF}}$, but falls behind. As will be shown later, such time delays between the two cold gas budgets, as well as between the global SFR and the cold *non-SF* gas content, are universally present during the episodic star-formation evolution of galaxies – a natural consequence of the cold gas reservoir taking time to gradually build up and form stars through compaction.

The third panel shows the evolution of metallicity in both *star-forming* gas and cold *non-SF* gas, denoted as Z_{SF} (solid) and $Z_{\text{cold, non-SF}}$ (dashed), respectively. It is interesting to note that the three sets of major peaks

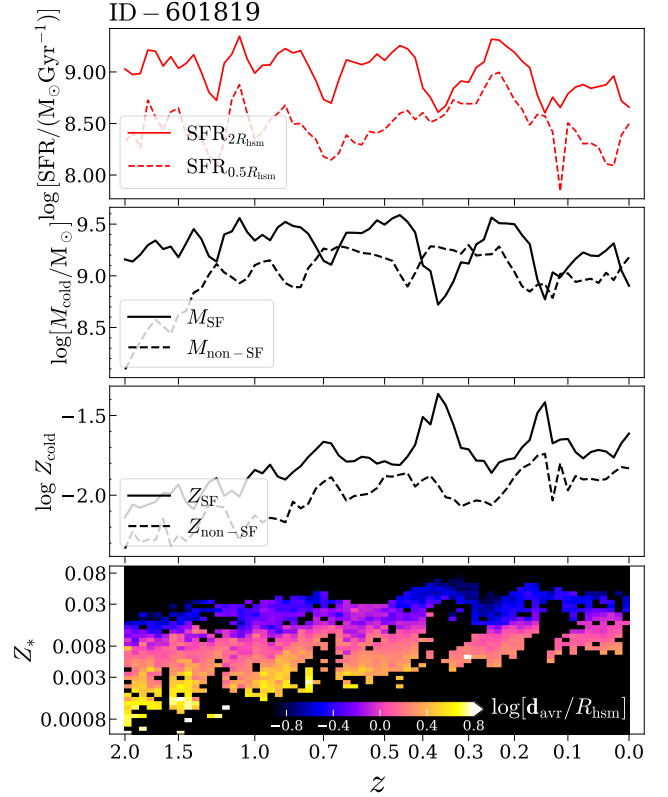


Figure 3. The episodic star-formation history and property evolution for one sample galaxy (ID-601819). The top panel presents the temporal variation of $\text{SFR}_{\leq 2R_{\text{hsm}}}$ (global, in solid line) and $\text{SFR}_{\leq 0.5R_{\text{hsm}}}$ (central, in dashed line). The second panel presents the evolution of cold gas mass within $2R_{\text{hsm}}$ for the *star-forming* gas (M_{SF} , solid line) and the cold *non-SF* gas ($M_{\text{cold, non-SF}}$, dashed line). The third panel shows the metallicity evolution for both *star-forming* gas and cold *non-SF* gas, denoted as Z_{SF} (solid) and $Z_{\text{cold, non-SF}}$ (dashed). The bottom panel presents the distribution of newly-formed stars at redshift z with stellar metallicity Z_* . The color represents the mass-weighted average distance (from the galaxy center, normalized by R_{hsm}). We only plot those pixels that contain at least three stellar particles to avoid shot noise.

of the gas metallicity at around $z = 0.7$, $z = 0.4$ and $z = 0.2$ roughly correspond to the three valley features in $\text{SFR}_{\leq 2R_{\text{hsm}}}$, while the two wide valleys in gas metallicity (one between $z = 0.7 - 0.4$ and one between $z = 0.4 - 0.2$) also happen to correspond to the two major peaks in $\text{SFR}_{\leq 2R_{\text{hsm}}}$ in the top panel. If the evolutionary curves of the gas-phase metallicity are vertically flipped, they would largely resemble that of $\text{SFR}_{\leq 2R_{\text{hsm}}}$ (and in fact also the cold gas content in the second panel). This mirror behavior is especially notable for the metallicity of the star-forming gas (see also Torrey et al. 2019). This already indicates a close connection between gas metallicity, SFR, and the cold gas budget.

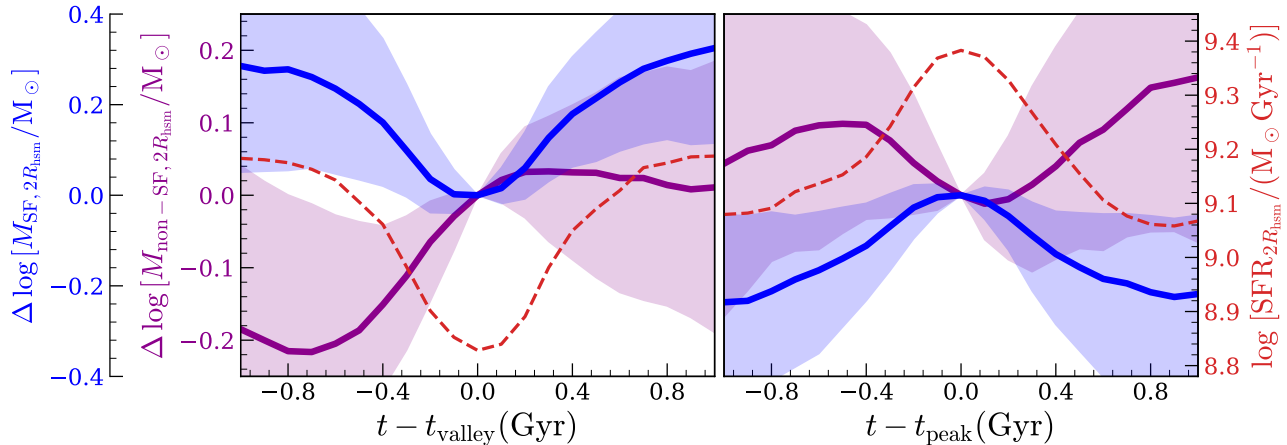


Figure 4. The relative mass $\Delta \log M$ within $2R_{\text{hsm}}$ of both *star-forming* gas (blue) and cold *non-SF* gas (magenta) as a function of time offset around the nearest peak/valley moment. In both panels, the shaded regions represent the central 68th percentile distribution. For clarity of visualization, the red dashed line marks the median SFR within $2R_{\text{hsm}}$.

We will investigate how such an episodic star-formation behavior can explain the observed fundamental metallicity relation (Mannucci et al. 2010) in the upcoming paper (Mei et al. in prep).

To further bring out the statistical behavior across our refined galaxy sample for trends akin to those exhibited by the example galaxy in Fig. 3, we stack the relative change in the logarithmic mass of the cold gas enclosed within $2R_{\text{hsm}}$ with respect to the values at SFR valleys and peaks as a function of time offset around these critical moments. The results are presented in Fig. 4. As can be seen, the rise and fall of the global SFR is roughly symmetric in time, i.e., the time it takes from valley to peak is about the same as that from peak to valley (both ~ 1 Gyr). As expected, we also see that the temporal variation of the relative *star-forming* gas mass $\Delta \log M_{\text{SF}}$ closely traces that of SFR, since the former is the birthplace of the latter.

However, the rise and fall of the relative cold *non-SF* gas mass $\Delta \log M_{\text{non-SF}}$ shows a significant time shift ahead of SFR. The upturn (downturn) of $\Delta \log M_{\text{non-SF}}$ from its minimum (maximum) starts $\sim 0.6 - 0.8$ Gyr before the upturn (downturn) of SFR. The buildup of this cold gas reservoir does not immediately raise SFR. This is because it takes time for this cold gas reservoir to be compressed, thus pushing a good fraction of it above the star-forming density threshold and turning it into star-forming gas. The decline of this reservoir also does not immediately reduce SFR. This can be explained by the fact that there is still the star-forming pool as a ‘buffer’ yet to be depleted due to star formation.

In return, star formation also impacts the cold *non-SF* gas reservoir. As can be seen, shortly after SFR commences rising from its valley, $\Delta \log M_{\text{non-SF}}$ reaches its maximum and starts declining – this gas reservoir from

now on starts being consumed or removed due to the combined effects of further compaction to form stars (through the phase of star-forming gas, which increases rapidly starting from this time) and the thermal and kinetic feedback processes as SFR goes up. As already explained, the continuous consumption of this cold gas reservoir does not immediately, but would eventually cause SFR to cease climbing up and then tip over, as star formation finally runs out of further cold gas supply. Shortly after this moment, with less active star formation and thus weaker feedback effects, this cold gas reservoir then manages to efficiently build up once again.

We note that the quantitative time delay as presented above indeed depends on the threshold value of $\Delta \log [\text{SFR}/\text{M}_{\odot} \text{Gyr}^{-1}]$ used for sample selection, which is presented in Fig. 11 in Appendix B (also see Section 2.3 for details). For a more detailed time analysis, we refer the reader to the next paper in this series (Mei et al. in prep).

3.3. Two branches of star formation and the retreat of newly-formed disk in each star-forming episode

As galaxies go through an episodic SFH, their sizes and metallicity distributions associated with the newly-formed stars also evolve accordingly. In the bottom panel of Fig. 3 we present the radial distribution of newly-formed stars at redshift z with stellar metallicity Z_* (for the example galaxy ID-601819). The color represents the mass-weighted average distance (from the galaxy center, normalized by R_{hsm}). For this 2D histogram, we only plot those pixels that contain at least three stellar particles to avoid shot noise. Several episodes of star formation are clearly present.

For this example galaxy, in each star formation cycle (defined as between two adjacent SFR valleys that sandwich a SFR peak at least 0.5 dex higher than the valleys, see Section 2.3 for details), since $z \sim 1$, two branches of star formation exist. One branch is related to central star formation ($\lesssim 0.5$ kpc) in higher-metallicity gas, which can always be on. In the second branch, a progression in a retreating/shrinking fashion is clearly present: a newer generation of stars very often forms initially at galaxy outskirts (at a few tens of kpc) as a result of cold gas accretion, which first arrives in disks at larger radii. With time, as the SFR gradually goes through the peak and starts decreasing, this round of star formation progressively born out of ever more metal-enriched gas, retreats inwards to the inner ~ 1 kpc region. Finally, towards the end of this episode, the next round of cold fresh gas accretion already kicks off at the galaxy’s outskirts, where new stars are born with lower metallicity. As a result, the intermittent pattern in the SFR is in fact more evident at galaxy outskirts (as indicated by yellowish colors), while star formation in the very central regions of galaxies (indicated by blueish colors) does not necessarily cease even at valleys of the global SFR. This can also be seen from the top panel of Fig. 3, where the episodic evolution of $\text{SFR}_{\leq 2R_{\text{hsm}}}$ is much more significant than that of $\text{SFR}_{\leq 0.5R_{\text{hsm}}}$.

Such a two-branch star-formation pattern, as well as a retreating/shrinking fashion of the outer star-formation branch during each episode, as demonstrated by the example galaxy, have been broadly observed among the progenitors of all 285 present-day star-forming disc galaxies (regardless of the adopted $\Delta \log [\text{SFR}/\text{M}_{\odot} \text{Gyr}^{-1}]$ threshold for the refined galaxy sample). Statistically, we shall also expect to see that the size of the stellar disc as measured by young stars shall grow around SFR valleys due to the arrival of fresh gas supply first at larger distances, and shrink around SFR peaks as star formation retreats to the central region. This is clearly demonstrated using galaxy sizes at the identified peaks and valleys for the refined galaxy sample in Fig. 5, which presents the histograms of the relative size increment $\Delta[R_{\text{hsm}, < 100 \text{ Myr}}/R_{\text{hsm}}]$ of stellar discs from the $(i-1)^{\text{th}}$ snapshot to the $(i+1)^{\text{th}}$ snapshot, where i is a snapshot number at either SFR valleys or peaks. Here we take all stellar particles younger than 100 Myr by that time to calculate their half-mass radius $R_{\text{hsm}, < 100 \text{ Myr}}$ and normalize this size by R_{hsm} to eliminate systematic differences between galaxies. As can be seen, on average, galaxies (as traced by newly formed stars) tend to grow larger around SFR valleys and become smaller around SFR peaks. We note that using R_{200} (the radius of the galaxy halo within which the av-

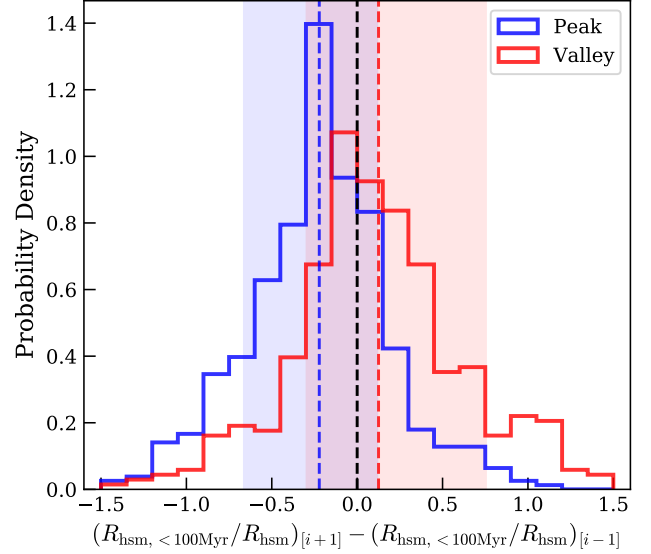


Figure 5. The histograms of the increment in normalized half-stellar-mass radius of young stars $R_{\text{hsm}, < 100 \text{ Myr}}/R_{\text{hsm}}$ from the $(i-1)^{\text{th}}$ snapshot to the $(i+1)^{\text{th}}$ snapshot, where i is a snapshot at either SFR valley or peak. The blue and red histograms represent the increment in normalized size around peaks and valleys, respectively. The dashed lines and shaded regions represent the corresponding median and central 68th percentile in each histogram. The black dashed line indicates the value of zero (representing no change in $R_{\text{hsm}, < 100 \text{ Myr}}/R_{\text{hsm}}$). Typically, the disk size of young stars grows around the time of the valley and becomes smaller around the time of the peak.

erage total matter density is 200 times the critical density of the universe at that time) for normalization has no qualitative impact on the result. We mention in passing that the distribution of newly-formed/young stars may thus vary during different epochs of star formation. Such a temporal variation may potentially contribute to scatter in galaxy sizes, particularly as observed at UV wavelengths.

3.4. Differential metallicity distributions of gas and young stars between SFR peaks and valleys

When further taking metallicity into account, the two branches of star formation during each episode are clearly revealed by the metallicity distributions of the younger stellar population and of star-forming gas. The former is presented in Fig. 6. Here again, ‘young stars’ are approximated by stellar particles with age younger than 100 Myr, and their metallicity is denoted as $\log Z_{*, < 100 \text{ Myr}}$. In the left panel, the blue and red histograms present the distributions of $\log Z_{*, < 100 \text{ Myr}}$ at SFR peaks and valleys, respectively. The darker and lighter shaded areas represent the distributions calculated within and outside $2R_{\text{hsm}}$, respectively. As can

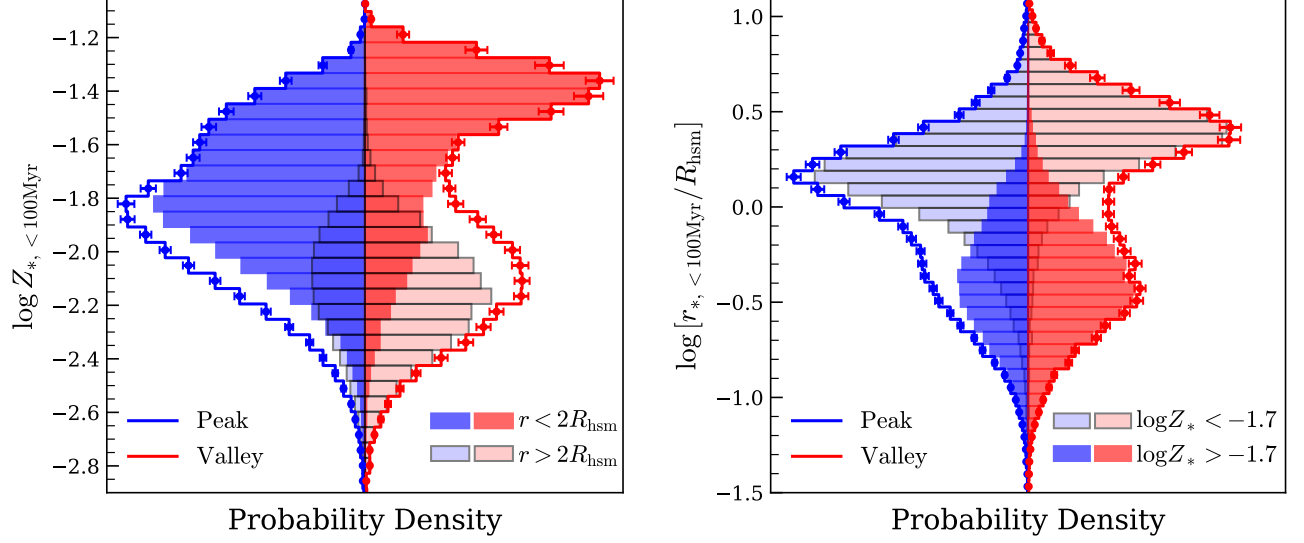


Figure 6. *Left Panel:* The mass-weighted metallicity distribution of young stars, $\log Z_{*, <100 \text{ Myr}}$, stacked at SFR peaks (blue) and valleys (red). The error bars represent the standard errors of the mean. The darker and lighter shaded regions represent the distributions of averaged young stellar metallicity calculated within and outside $2R_{\text{hsm}}$. *Right Panel:* The mass-weighted distribution of normalized galactocentric radii of young stellar, $\log [r_{*, <100 \text{ Myr}} / R_{\text{hsm}}]$. The darker and lighter shaded regions represent the distributions calculated with $\log Z_{*, <100 \text{ Myr}} > -1.7$ and < -1.7 , respectively.

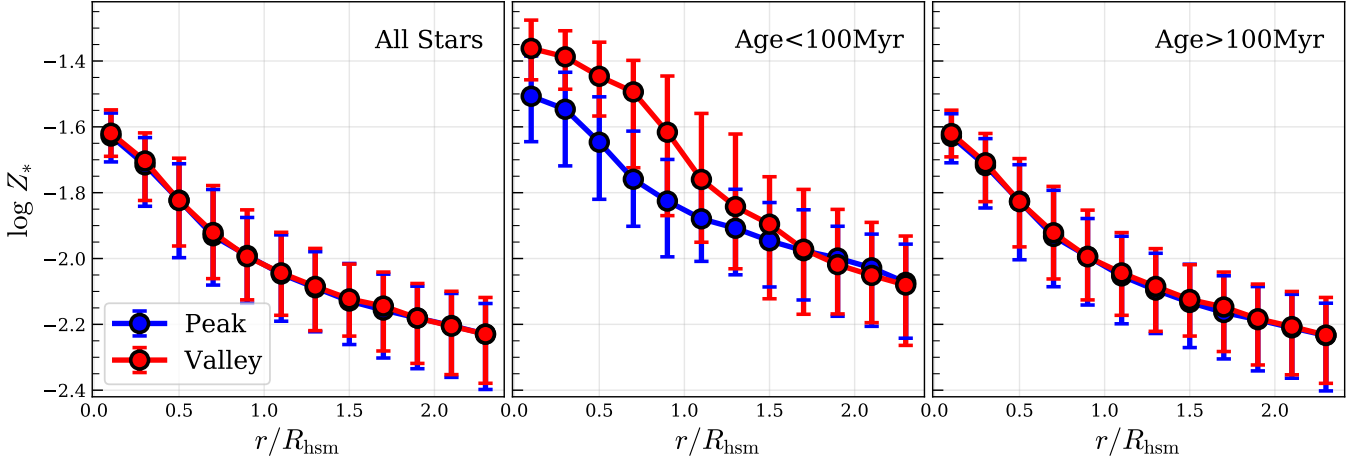


Figure 7. The radial profiles of the stellar metallicity from all stars (left), stars with ages younger than 100 Myr (middle), and stars older than 100 Myr (right). In each panel, the blue and red colors correspond to the time of peak and valley, respectively, where the error bars show the central 68th percentile distributions. For the younger stellar population, the metallicity profiles are less concentrated at SFR peaks compared to valleys.

be seen, the overall distribution of $\log Z_{*, <100 \text{ Myr}}$ measured at SFR valleys clearly exhibits bimodality, with a higher (lower) metallicity peak corresponding to the inner (outer) star-formation region. To the contrary, the overall distribution of $\log Z_{*, <100 \text{ Myr}}$ at SFR peaks exhibits a broad shape which is largely dominated by star formation within $2R_{\text{hsm}}$. In the right panel, the histograms present the distributions of galactocentric distance $\log [r_{*, <100 \text{ Myr}} / R_{\text{hsm}}]$ of young stars at SFR peaks

and valleys. The darker and lighter shaded areas now represent the radial distributions of young stars with $\log Z_{*, <100 \text{ Myr}} > -1.7$ and < -1.7 , respectively. As can be seen, at both epochs (peak and valley), the distributions exhibit bimodality to a certain degree. Young stars with lower metallicity tend to reside in galaxy outskirts (peak at $2-3R_{\text{hsm}}$), while young stars with higher metallicity tend to occupy the central regions (peak at $\sim 0.3R_{\text{hsm}}$).

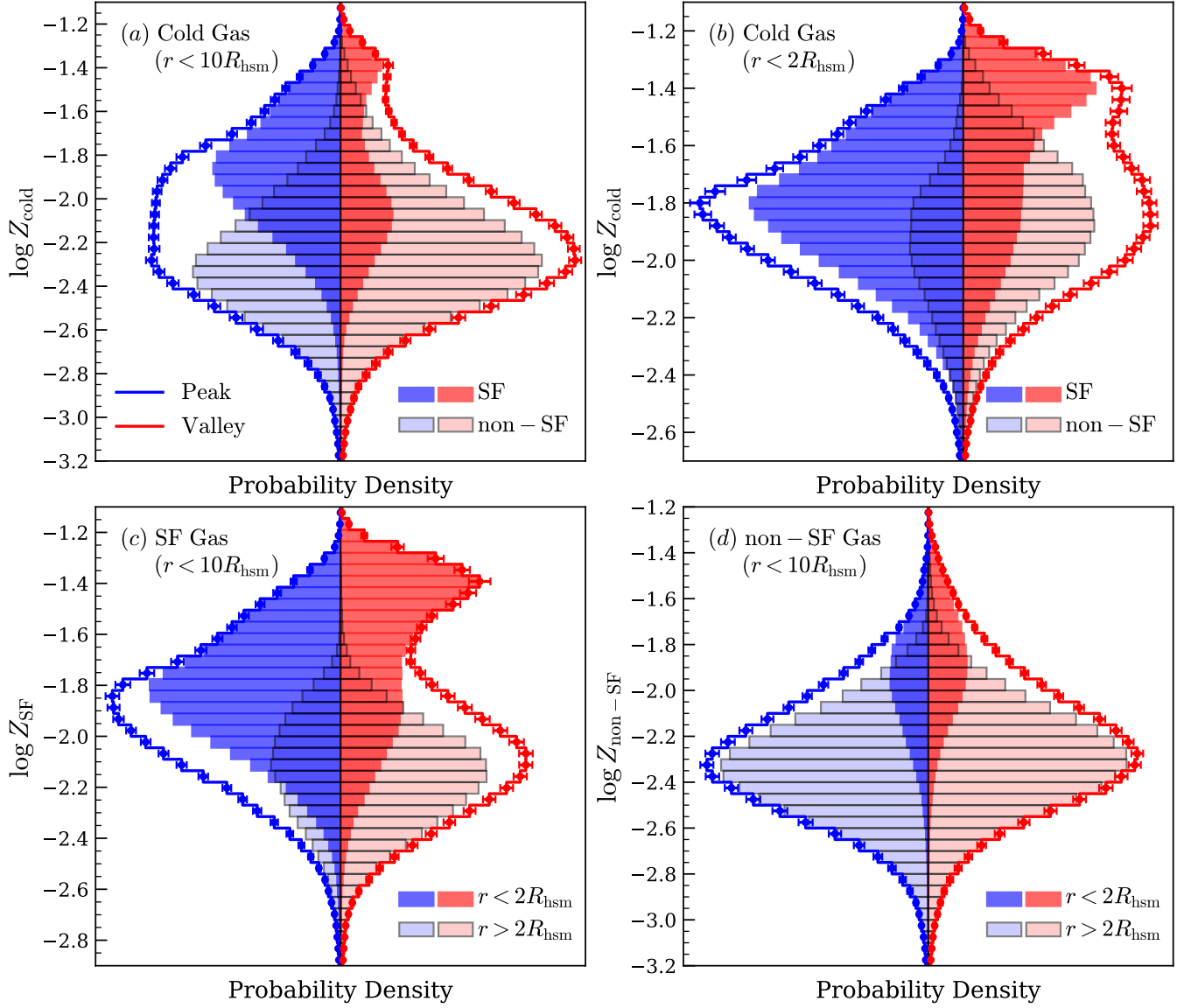


Figure 8. (a): The stacked histogram of average mass-weighted total cold gas metallicity, $\log Z_{\text{cold}}$, at SFR peaks (blue) and valleys (red) within $10R_{\text{hsm}}$. The darker and lighter shaded regions represent the distributions calculated for *star-forming* and cold *non-SF* gas, respectively. Plotting style similar to Fig. 6. (b): Similar to panel (a), but evaluating within $2R_{\text{hsm}}$. (c): The stacked histogram of average mass-weighted *star-forming* gas metallicity, $\log Z_{\text{SF}}$, at SFR peaks (blue) and valleys (red) within $10R_{\text{hsm}}$. The darker and lighter shaded regions represent the metallicity histograms within and outside $R = 2R_{\text{hsm}}$, respectively. (d): Similar to panel (c), but calculated for metallicity $\log Z_{\text{non-SF}}$ of the cold *non-SF* gas.

Such behaviors of the young-star metallicity distribution originate from their different spatial distributions at SFR peaks and valleys due to the presence of two star-formation branches. It is worth noting that the younger stellar population at SFR peaks in general extends to a smaller distance and is less concentrated and of lower metallicity (in particular at distances within $2R_{\text{hsm}}$), in comparison to at SFR valleys. This can be more clearly seen in Fig. 7, which presents the radial profiles of stellar metallicity from all stars (left), stars younger than 100 Myr (middle), and stars older than 100 Myr (right).

Blue and red colors correspond to SFR peaks and valleys, respectively. As can be seen, metallicity profiles from the entire stellar population are dominated by the older stellar population and show no difference between the peak and valley moments. However, for the younger stellar population, a clear difference is observed: within $2R_{\text{hsm}}$, young star metallicity is significantly lower at SFR peaks than at valleys – a natural consequence of stars born out of the freshly replenished gas with lower metallicity.

The gas-phase metallicity distributions presented in Fig. 8 also reveal the presence of two star-formation branches during the episodic evolution. The top panels show the stacked mass-weighted total cold gas metallicity, $\log Z_{\text{cold}}$, at SFR peaks (blue) and valleys (red) within $10R_{\text{hsm}}$ and $2R_{\text{hsm}}$. The darker and lighter shaded regions represent the distributions calculated for *star-forming* and cold *non-SF* gas, respectively. As can be seen, within $10R_{\text{hsm}}$ the cold but *non-SF* gas contributes to the total cold gas budget with a higher fraction than *star-forming* gas, in particular (with a dominating fraction) at SFR valleys. Within $2R_{\text{hsm}}$, *star-forming* gas dominates the total cold gas budget at SFR peaks while the cold *non-SF* gas contributes with a higher fraction at SFR valleys (which can also be seen in Fig. 3). We note that at the valley moments, the cold gas reservoir has already started building up, prior to an enhanced star formation kicking off (see Fig. 4). In addition, the cold but *non-SF* gas in general exhibits a lower metallicity than the *star-forming* gas at both SFR peaks and valleys, which is a result of the combination of fresh gas replenishment first at the cold gas reservoir (i.e., *non-SF*) and feedback and chemical enrichment to the star-forming gas pool.

The bottom two panels show similar histograms to the top two panels, but evaluated for the *star-forming* (left) and the cold *non-SF* (right) gas within $10R_{\text{hsm}}$, respectively. At this time, the darker and lighter shaded regions represent the metallicity histograms within and outside $R = 2R_{\text{hsm}}$. As can be seen, for both gas components, gas located at galaxy outskirts ($r > 2R_{\text{hsm}}$) in general possesses lower metallicity than in the inner region ($r < 2R_{\text{hsm}}$), which is a similar behavior as for the younger stellar population. In addition, similar to the left panel of Fig. 6, the metallicity of *star-forming* gas also exhibits a clear bimodal distribution at SFR valleys, composed of a higher-metallicity branch in the inner regions and a lower-metallicity branch at the outskirts. This is also the consequence of two branches of star formation, as already described above. We mention in passing that measurements of the cold-gas metallicity probability distributions for both gas components and in both inner and outer regions of galaxies may provide good evidence of the star-formation phase that a galaxy is in.

4. RESULTS: SCATTER OF SFMS

Across the episodic SFH of present-day SFMS galaxies, many properties vary as SFR changes in time. However, these properties fluctuate more or less about a quasi-equilibrium state (e.g., Forbes et al. 2014; Torrey et al. 2019; De Lucia et al. 2020; van Loon et al. 2021.

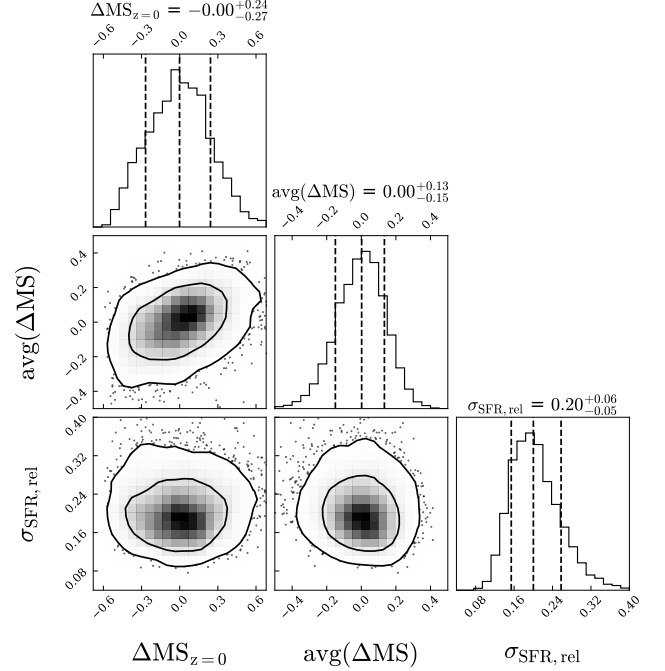


Figure 9. The correlation between the main-sequence offset at $z = 0$ ($\Delta\text{MS}_{z=0}$), the historically averaged main-sequence offset since $z = 1$ ($\text{avg}(\Delta\text{MS})$) and the temporal fluctuation of individual galaxies since $z = 1$ ($\sigma_{\text{SFR,rel}}$). The SFR is measured within $2R_{\text{hsm}}$. The 16-50-84 percentile of each quantity is shown above the corresponding panel.

Therefore, we expect that the episodic star-formation behavior causing temporal fluctuation in SFR should be able to (at least partially) explain the SFMS scatter today. For present-day ($z = 0$) star-forming galaxies in the TNG100, we determine the ridge of the SFMS and report the 16-50-84 percentile of their main-sequence offset $\Delta\text{MS}_{z=0}$ is $-0.001^{+0.243}_{-0.258}$ dex. In comparison, the 16-50-84 percentile of ΔMS among all galaxy progenitors since $z \sim 1$ is $0.006^{+0.245}_{-0.272}$ dex, exhibiting a scatter consistent with that of the SFMS at $z = 0$. This likeness indicates that the SFMS scatter does not show appreciable evolution from $z \sim 1$ to the present day.

As the evaluation of the intrinsic differentiation between galaxies, the 16-50-84 percentile of the historically averaged main-sequence offset since $z = 1$, $\text{avg}(\Delta\text{MS})$, is $0.002^{+0.131}_{-0.145}$ dex. In addition, the 16-50-84 percentile of the temporal SFR fluctuations within individual galaxies around their long-term average, $\sigma_{\text{SFR,rel}}$, is $0.200^{+0.058}_{-0.046}$ dex (for sample selection and detailed definitions, see Section 2.2). These statistics reveal that the SFMS scatter (on the order of **0.25** dex) can be well accounted for by the temporal fluctuation in SFR (on the order of **0.2** dex) within individual galaxies, plus a galaxy-to-galaxy differentiation (on the order of **0.15** dex) in long-term averaged SFR (see also Matthee &

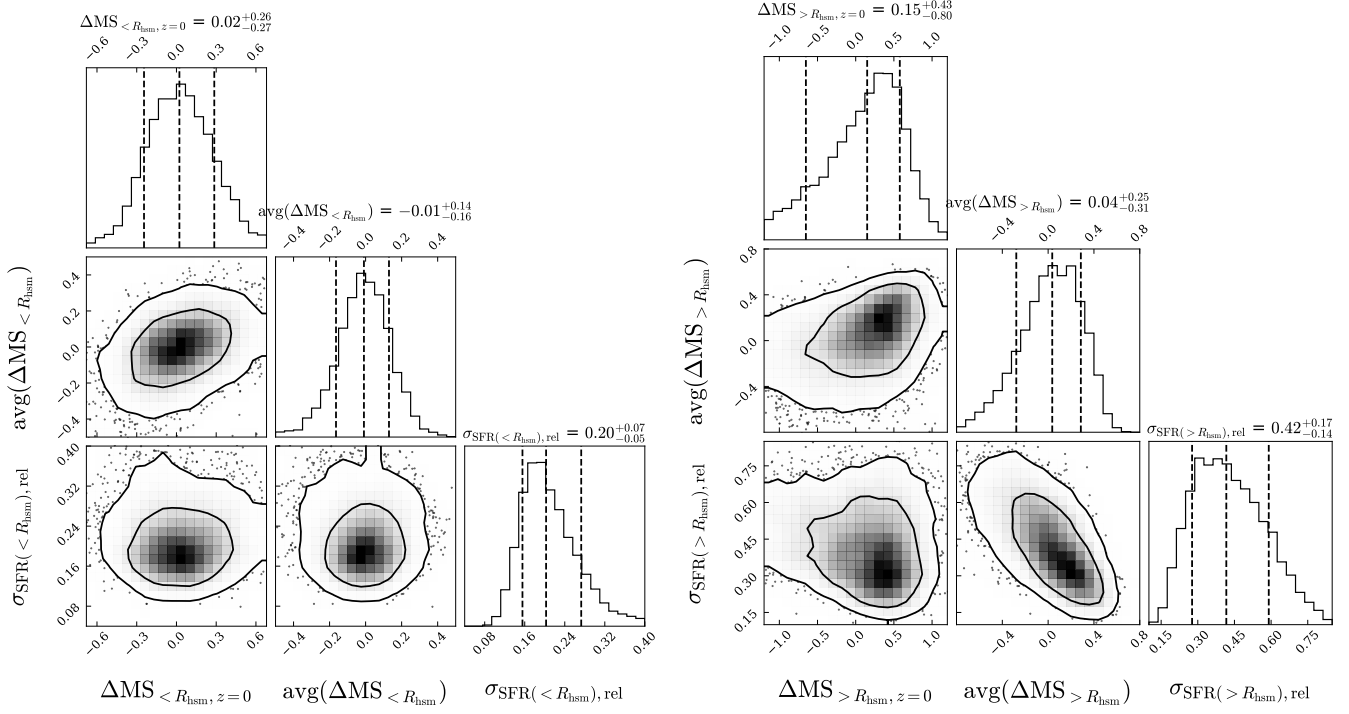


Figure 10. *Left Panel:* Similar to Fig. 9 except that the SFR is measured within R_{hsm} . The main-sequence offset $\Delta MS_{<R_{\text{hsm}}}$ is recalculated from the newly-fitted ridge, and the temporal SFR fluctuation of individual galaxies $\sigma_{\text{SFR}(<R_{\text{hsm}}),\text{rel}}$ is also taken from the re-fitted long-term evolution for each galaxy. *Right Panel:* Similar to the left panel except that the SFR is measured in an annulus between R_{hsm} and $2R_{\text{hsm}}$.

Schaye 2019; Blank et al. 2021; Wan et al. 2025). Assuming the ergodicity of the SFMS, Wang & Lilly (2022b) also found a larger contribution from the temporal fluctuation in SFR to the scatter of SFMS, based on the observed SFMS scatter derived on two different timescales.

It is then interesting to consider whether galaxies that live above (below) the main-sequence ridge today have, on average, lived above (below) the ridge in their history, and whether a strong correlation exists between the historically averaged main-sequence offset $\text{avg}(\Delta MS)$ and the temporal fluctuation $\sigma_{\text{SFR,rel}}$. To answer this question, we present Fig. 9. This corner plot shows the correlation between $\Delta MS_{z=0}$, $\text{avg}(\Delta MS)$ and $\sigma_{\text{SFR,rel}}$. We find a positive correlation between present-day main-sequence offset $\Delta MS_{z=0}$ and historical averaged main-sequence offset since $z \sim 1$ ($\text{avg}(\Delta MS)$), indicating that galaxies with higher (lower) ΔMS at $z = 0$ tend to reside above (below) SFMS from $z \sim 1$. This result echoes a recent observational result from Wan et al. (2025), conducted for 1928 star-forming galaxies from the LEGA-C survey. In comparison, correlation between $\text{avg}(\Delta MS)$ and $\sigma_{\text{SFR,rel}}$ is insignificant. We note that in this study, we aim at understanding the key processes during the episodic evolution and how this causes a given population of galaxies to appear with diverse observed properties. We have not answered what physical origins have

led to the intrinsic differences among galaxies or what physical processes have largely determined the amplitude of the temporal fluctuation. We leave these investigations to future work of this series (Gui et al. in prep).

As presented in Section 3.3, star-formation that happens at inner regions of galaxies and that at the outskirts also follow markedly different evolutionary patterns. A related question worth asking is then how the above-investigated SFR properties depend on the (projected) spatial region within which they are evaluated. To answer this question, we carry out the same analysis but considering the star formation within an aperture, SFR_{apt} , evaluated (1) within a radius of R_{hsm} from the galaxy center, and (2) within an annulus between R_{hsm} and $2R_{\text{hsm}}$. In each case, the SFMS galaxy sample remains the same. However, we re-fit the main sequence ridge at different redshifts using SFR_{apt} (instead of global SFR), and re-calculate the offset from the ridge as $\text{avg}(\Delta MS_{\text{apt}})$. For the temporal fluctuation $\sigma(\text{SFR}_{\text{apt}})$, we re-fit a linear relation using $\log \text{SFR}_{\text{apt}} - \log(1+z)$ and take the linear prediction as the mean to calculate $\sigma(\text{SFR}_{\text{apt}})$. Fig. 10 presents the results similar to Fig. 9 but for SFR evaluated within two different regions. The left panel shows the distributions and correlations with SFR measured within R_{hsm} , while the right panel shows

those with SFR evaluated in the annulus between R_{hsm} and $2R_{\text{hsm}}$.

As can be seen, the results for SFR_{apt} measured within R_{hsm} very much resemble those using global SFR (as presented in Fig. 9), indicating that the global feature is largely dominated by the condition within R_{hsm} . However, the results for SFR_{apt} measured between R_{hsm} and $2R_{\text{hsm}}$ differ substantially from the former cases. Firstly, $\Delta\text{MS}_{z=0}$ no longer exhibits a symmetric distribution around $\Delta\text{MS} = 0$ (the new ridge), but with a long tail bias towards lower values in ΔMS . Secondly, using SFR evaluated between R_{hsm} and $2R_{\text{hsm}}$ (i.e., at galaxy outskirts), the scatter of $\text{avg}(\Delta\text{MS})$ as well as $\sigma_{\text{SFR,rel}}$ have all become significantly larger than those evaluated within the central R_{hsm} . This can be attributed to the fact that the episodic evolution at galaxy outskirts is more prominent than in inner regions (as demonstrated in Section 3.3) thus causing larger scatters. Finally, we also mention in passing that for SFR measured at such larger radii, $\text{avg}(\Delta\text{MS})$ and $\sigma_{\text{SFR,rel}}$ now exhibit a strong negative correlation, i.e., galaxies with lower $\text{avg}(\Delta\text{MS})$ tend to have a larger temporal fluctuation of $\sigma_{\text{SFR,rel}}$. This result is likely attributed to the steep decline of SFR in the outskirts at some specific epochs, which elevates $\sigma_{\text{SFR,rel}}$ and suppresses $\text{avg}(\Delta\text{MS})$ simultaneously. We defer the investigation of the detailed physical origin to an upcoming paper (Gui et al. in prep).

5. CONCLUSIONS AND DISCUSSIONS

This paper is a follow-up study of Wang et al. (2022), with a more focused and detailed investigation of the episodic SFH of present-day SFMS galaxies since $z \sim 1$. The goal of this study is to present an overview of the episodic star formation scenario and investigate how well the resulting temporal variation in SFR can account for the observed scatter of the star-forming main sequence at $z = 0$. This is achieved through tracing back in time the history of star-forming galaxies at $z = 0$ in the TNG100 simulation and investigating the co-evolution of the size, metallicity, and radial distribution of young stars and cold gas, as the galaxies go through SFR peaks and valleys in the past 7 – 8 Gyrs. In particular, we split the cold gas into a *non-star-forming* gas reservoir and a *star-forming* gas pool (see Section 2.4 for detailed definitions and the method), and investigate the different stellar and gas properties at typical SFR peaks and valleys (see Section 2.5). Our main results about the episodic SFH and its impact on scatter in SFMS are listed below:

- During each episode, two branches of star formation exist. While one star-formation branch happens in heavily polluted gas in the inner region

(and in many cases remains always on), a secondary star-formation branch starts from lower-metallicity regions at galaxy outskirts where fresh gas first arrives, and gradually retreats to the centers of galaxies. This picture is consistent with the coplanar inflow model proposed by Wang & Lilly (2022b, 2023a,b); Lyu et al. (2025). As a consequence, the intermittent pattern in SFR is more prominent at galaxy outskirts, while star formation in inner regions does not necessarily cease even at valleys of global SFR (see Fig. 3 and Section 3.3).

- The relative stellar size of the younger stellar population (star-forming age younger than 100 Myr) $R_{\text{hsm}, < 100\text{Myr}}/R_{\text{hsm}}$ systematically increases around SFR valleys, and decreases around SFR peaks, as a result of stellar disc growth (for the outer-branch star-formation) first at larger radii at the beginning of each star-formation episode (i.e., SFR valley), followed up by a ‘shrinkage’ after the peak time (see Fig. 5 and Section 3.3). This temporal variation in the radial extent of young stars is anticipated to contribute to the scatter in galaxy sizes as observed at UV wavelengths (although the latter may be modulated by spatially varying attenuation; see Zhang et al. 2023).
- Statistically, the younger stellar populations in galaxies at SFR *valleys* exhibit a strong bimodal probability distribution function (PDF) in metallicity, which is composed of a higher and a lower metallicity peak corresponding to the inner ($r < 2R_{\text{hsm}}$) and the outer ($r > 2R_{\text{hsm}}$) star-formation region, respectively (Fig. 6). The younger stellar population at SFR peaks possesses systematically lower metallicity than at SFR valleys across the galaxy radial range within $2R_{\text{hsm}}$ as a result of fresh gas replenishment. The total stellar population, however, does not reveal noticeable differences between the peaks and valleys (see Fig. 7 and Section 3.4).
- Similarly, the two branches of star formation as well as the retreating fashion of disk growth as the SFR rises from valley to peak also leaves different observational imprints on the distribution of the cold-gas metallicity (for both the *non-SF* gas reservoir and the *star-forming* gas pool) as measured in both inner and outer regions of galaxies. In particular, bimodal PDFs in *star-forming* gas metallicity are prominent at SFR *valleys* due to the co-existence of star-forming gas with dis-

tinct chemical signatures associated with two star-forming branches (Fig. 8 and Section 3.4).

- The 16-50-84 percentile of the star formation main sequence offset (ΔMS) at $z = 0$ is $-0.001^{+0.243}_{-0.258}$ dex and the historical main sequence offset ΔMS among all of the galaxy progenitors since $z \sim 1$ is $0.006^{+0.245}_{-0.272}$ dex, indicating the MS scatter does not show appreciable evolution from $z = 1$ to the present day. Among individual galaxies and their progenitors since $z \sim 1$, the historically averaged ΔMS is $0.002^{+0.131}_{-0.145}$ dex, while the 1σ of temporal fluctuation within each galaxy is ΔMS is $0.200^{+0.058}_{-0.046}$ dex. These statistics support the idea that the galaxies are going through episodic SFH about a quasi-equilibrium state, the temporal fluctuation in SFR (on the order of 0.2 dex) together with intrinsic differentiation between galaxies (on the order of 0.15 dex) can explain $z = 0$ SFMS scatter (on the order of 0.25 dex) (see Fig. 9 and Section 4).

We note that the conclusions presented above are entirely based on the TNG100 simulation. As the episodic star-formation behavior is a combined consequence of both external gas replenishment and internal feedback processes, the details of such behaviors are surely sub-

ject to the adopted feedback models by the simulation. In addition, the results also indicate that such an episodic star-formation scenario can partially explain the observed scatter of the SFMS. It will be highly interesting to see whether different cosmological simulations of this kind shall provide consistent answers and thus agree in this aspect.

ACKNOWLEDGEMENTS

We acknowledge Dr. Sen Wang, Profs. Volker Springel, Huiyuan Wang, Jing Wang, Yong Shi and Xiaoyang Xia for their constructive and insightful suggestions. This work is supported by the National Key Research and Development Program of China (Grant No. 2022YFA1602903), the National Natural Science Foundation of China (Grant No. 12433003), and the China Manned Space Project (No. CMS-CSST-2025-A10). This work acknowledges the Tsinghua Astrophysics High-Performance Computing platform for providing the computational and storage resources that supported this research. The authors gratefully acknowledge support from the Royal Society International Exchanges scheme (IES\R2\242195). SW acknowledges support from China's National Foreign Expert programme (H20240871).

Software: Astropy (Astropy Collaboration et al. 2013, 2018, 2022), Matplotlib (Hunter 2007), Numpy (Harris et al. 2020), Scipy (Virtanen et al. 2020)

APPENDIX

A. PEAK-VALLEY PAIR SEARCHING ALGORITHM

Here we present the peak-valley pair searching algorithm in detail. Given an SFR series of an individual galaxy, we first identify local maxima and minima by comparing each snapshot with its two immediate predecessors and two immediate successors (about 0.2 Gyr between adjacent snapshots), respectively. We then search for downward peak-valley pairs and upward valley-peak pairs that satisfy $\Delta \log [\text{SFR}/\text{M}_\odot \text{Gyr}^{-1}]$ greater than a given threshold (e.g., 0.5 dex) since $z \sim 1$.

Taking the upward valley-peak pair search for an example, the algorithm will be interpreted step by step:

1. First, we start from the first minimum since $z \sim 1$ and label it as the valley candidate.
2. Then, we go forward in time for every minima and maxima in order and try to find a matching peak candidate that satisfies the threshold mentioned before. Several cases will be encountered during the process:
 - (a) If, before finding an eligible peak candidate, another minimum lower than the initial minimum appears, we update the valley candidate to this lower one.
 - (b) If a satisfied maximum is found, we label this maximum as the peak candidate. However, we will continue searching to see if there exists a maximum with an even greater difference. The purpose of this step is to dampen the effect of minor fluctuations and capture more significant signals. If so, we update the peak candidate to this new maximum.
 - (c) The search process stops when the peak candidate exists and a further minimum is encountered such that the difference between this further minimum to the current peak candidate is comparable to that between

the existing valley candidate to the current peak candidate (we set the ratio between the former and the latter to be larger than 0.7, i.e., $\text{SFR}_{\text{peak}} - \text{SFR}_{\text{new min}} > 0.7 \times (\text{SFR}_{\text{peak}} - \text{SFR}_{\text{valley}})$). Then, the current peak candidate and existing valley candidate will finally be recorded as an upward valley-peak pair. Setting this ratio to other value larger than 0.5 would not qualitatively change our results and conclusion.

3. Subsequently, the next starting valley will be selected as the first valley following the peak in the last pair, ensuring that pairs do not overlap.

The procedure for identifying downward peak-valley pairs is analogous to that for the upward valley-peak pairs described above. For each galaxy, we search for both upward (i.e., valley-to-peak) pairs and downward (i.e., peak-to-valley) pairs. Among the total of 285 galaxies, 191 galaxies have experienced at least two upward or two downward pairs that satisfy $\Delta \log [\text{SFR}/\text{M}_{\odot} \text{Gyr}^{-1}] > 0.5$ dex since $z \sim 1$, which we consider to indicate the presence of at least two episodes.

B. DIFFERENT THRESHOLDS FOR PEAK-VALLEY PAIRS

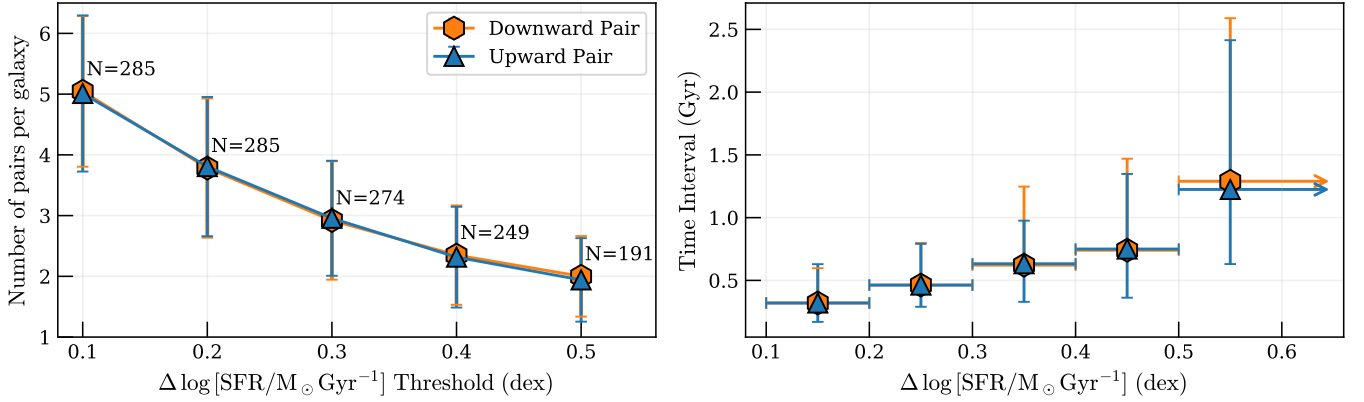


Figure 11. *Left Panel:* The number of pairs per galaxy as a function of $\Delta \log [\text{SFR}/\text{M}_{\odot} \text{Gyr}^{-1}]$ threshold. Blue triangles represent the upward pairs, and orange hexagons represent the downward pairs. At each threshold, the number of galaxies that possess such episodic star-forming features is also labeled beside the symbol. *Right Panel:* The median and central 68th percentiles of time intervals of the pairs in different $\Delta \log [\text{SFR}/\text{M}_{\odot} \text{Gyr}^{-1}]$ bins with 0.1 dex interval, except for the last bin, where no upper bound is set for this bin. In this work, since we choose 0.5 dex as a threshold, the typical peak-valley timescale is ~ 1.25 Gyr.

In this study, we only take galaxies that possess peak-valley pairs with $\Delta \log [\text{SFR}/\text{M}_{\odot} \text{Gyr}^{-1}] > 0.5$ dex to further compose a refined galaxy sample for peak-valley statistics (see Section 2.3 for details). Here, we also present how the number of peak-valley pairs per galaxy and the time intervals in between depend on the different choices of the threshold.

In the left panel of Fig. 11, we show the number of pairs per galaxy, given an adopted $\Delta \log [\text{SFR}/\text{M}_{\odot} \text{Gyr}^{-1}]$ threshold. As can be seen, all 285 star-forming rotating disc galaxies in our sample on average have five downward or upward peak-valley pairs that are separated by at least $\Delta \log [\text{SFR}/\text{M}_{\odot} \text{Gyr}^{-1}] > 0.1$ dex. The number of pairs decreases as the threshold increases. When increasing the threshold to 0.5 dex, the number of galaxies is reduced to 191, which have experienced twice such peak-valley star-formation episodes on average.

In addition, we also expect that smaller (larger) SFR temporal fluctuations happen on shorter (longer) timescales. This can be clearly seen in the right panel of Fig. 11, which presents the 16-50-84 percentiles of time intervals between the identified peaks and valleys of pairs that meet the requirement of $\Delta \log [\text{SFR}/\text{M}_{\odot} \text{Gyr}^{-1}]$. For the majority of galaxies that satisfy $\Delta \log [\text{SFR}/\text{M}_{\odot} \text{Gyr}^{-1}]$ below 0.4 dex, the peak-valley timescale is around 0.5 Gyr. While with $\Delta \log [\text{SFR}/\text{M}_{\odot} \text{Gyr}^{-1}] > 0.5$ dex, the resulting galaxy sample shows a typical peak-valley timescale of ~ 1.25 Gyr. The smaller $\Delta \log [\text{SFR}/\text{M}_{\odot} \text{Gyr}^{-1}]$, the shorter the peak-valley time interval. Through visual inspection over all 285 star-forming rotating disc galaxies we confirm that the reported two branches of star formation with a retreating/shrinking

disk growing fashion are universal among this population, regardless of the $\Delta \log [\text{SFR}/\text{M}_\odot \text{Gyr}^{-1}]$ threshold adopted (see Section 3 for details).

REFERENCES

- Anglés-Alcázar, D., Faucher-Giguère, C.-A., Quataert, E., et al. 2017, *MNRAS*, 472, L109, doi: [10.1093/mnras/slx161](https://doi.org/10.1093/mnras/slx161)
- Astropy Collaboration, Robitaille, T. P., Tollerud, E. J., et al. 2013, *A&A*, 558, A33, doi: [10.1051/0004-6361/201322068](https://doi.org/10.1051/0004-6361/201322068)
- Astropy Collaboration, Price-Whelan, A. M., Sipőcz, B. M., et al. 2018, *AJ*, 156, 123, doi: [10.3847/1538-3881/aabc4f](https://doi.org/10.3847/1538-3881/aabc4f)
- Astropy Collaboration, Price-Whelan, A. M., Lim, P. L., et al. 2022, *ApJ*, 935, 167, doi: [10.3847/1538-4357/ac7c74](https://doi.org/10.3847/1538-4357/ac7c74)
- Bahé, Y. M., & McCarthy, I. G. 2015, *MNRAS*, 447, 969, doi: [10.1093/mnras/stu2293](https://doi.org/10.1093/mnras/stu2293)
- Baldry, I. K., Glazebrook, K., Brinkmann, J., et al. 2004, *ApJ*, 600, 681, doi: [10.1086/380092](https://doi.org/10.1086/380092)
- Balogh, M. L., Baldry, I. K., Nichol, R., et al. 2004, *ApJL*, 615, L101, doi: [10.1086/426079](https://doi.org/10.1086/426079)
- Barnes, J. E., & Hernquist, L. E. 1991, *ApJL*, 370, L65, doi: [10.1086/185978](https://doi.org/10.1086/185978)
- Behroozi, P., Wechsler, R. H., Hearin, A. P., & Conroy, C. 2019, *MNRAS*, 488, 3143, doi: [10.1093/mnras/stz1182](https://doi.org/10.1093/mnras/stz1182)
- Bell, E. F., Wolf, C., Meisenheimer, K., et al. 2004, *ApJ*, 608, 752, doi: [10.1086/420778](https://doi.org/10.1086/420778)
- Blank, M., Meier, L. E., Macciò, A. V., et al. 2021, *MNRAS*, 500, 1414, doi: [10.1093/mnras/staa2670](https://doi.org/10.1093/mnras/staa2670)
- Brinchmann, J., Charlot, S., White, S. D. M., et al. 2004, *MNRAS*, 351, 1151, doi: [10.1111/j.1365-2966.2004.07881.x](https://doi.org/10.1111/j.1365-2966.2004.07881.x)
- Budavári, T., Connolly, A. J., Szalay, A. S., et al. 2003, *ApJ*, 595, 59, doi: [10.1086/377168](https://doi.org/10.1086/377168)
- Caplar, N., & Tacchella, S. 2019, *MNRAS*, 487, 3845, doi: [10.1093/mnras/stz1449](https://doi.org/10.1093/mnras/stz1449)
- Cattaneo, A., Faber, S. M., Binney, J., et al. 2009, *Nature*, 460, 213, doi: [10.1038/nature08135](https://doi.org/10.1038/nature08135)
- Cenci, E., Feldmann, R., Gensior, J., et al. 2024, *MNRAS*, 527, 7871, doi: [10.1093/mnras/stad3709](https://doi.org/10.1093/mnras/stad3709)
- Ceverino, D., & Klypin, A. 2009, *ApJ*, 695, 292, doi: [10.1088/0004-637X/695/1/292](https://doi.org/10.1088/0004-637X/695/1/292)
- Cicone, C., Maiolino, R., & Marconi, A. 2016, *A&A*, 588, A41, doi: [10.1051/0004-6361/201424514](https://doi.org/10.1051/0004-6361/201424514)
- Cicone, C., Maiolino, R., Sturm, E., et al. 2014, *A&A*, 562, A21, doi: [10.1051/0004-6361/201322464](https://doi.org/10.1051/0004-6361/201322464)
- Ciesla, L., Elbaz, D., Ilbert, O., et al. 2024, *A&A*, 686, A128, doi: [10.1051/0004-6361/202348091](https://doi.org/10.1051/0004-6361/202348091)
- Ciotti, L., & Ostriker, J. P. 2007, *ApJ*, 665, 1038, doi: [10.1086/519833](https://doi.org/10.1086/519833)
- Conselice, C. J., Bershad, M. A., Dickinson, M., & Papovich, C. 2003, *AJ*, 126, 1183, doi: [10.1086/377318](https://doi.org/10.1086/377318)
- Cox, T. J., Jonsson, P., Primack, J. R., & Somerville, R. S. 2006, *MNRAS*, 373, 1013, doi: [10.1111/j.1365-2966.2006.11107.x](https://doi.org/10.1111/j.1365-2966.2006.11107.x)
- Croton, D. J., Springel, V., White, S. D. M., et al. 2006, *MNRAS*, 365, 11, doi: [10.1111/j.1365-2966.2005.09675.x](https://doi.org/10.1111/j.1365-2966.2005.09675.x)
- Daddi, E., Dickinson, M., Morrison, G., et al. 2007, *ApJ*, 670, 156, doi: [10.1086/521818](https://doi.org/10.1086/521818)
- De Lucia, G., Xie, L., Fontanot, F., & Hirschmann, M. 2020, *MNRAS*, 498, 3215, doi: [10.1093/mnras/staa2556](https://doi.org/10.1093/mnras/staa2556)
- Dekel, A., & Birnboim, Y. 2006, *MNRAS*, 368, 2, doi: [10.1111/j.1365-2966.2006.10145.x](https://doi.org/10.1111/j.1365-2966.2006.10145.x)
- Dekel, A., & Burkert, A. 2014, *MNRAS*, 438, 1870, doi: [10.1093/mnras/stt2331](https://doi.org/10.1093/mnras/stt2331)
- Dekel, A., & Silk, J. 1986, *ApJ*, 303, 39, doi: [10.1086/164050](https://doi.org/10.1086/164050)
- Dekel, A., Zolotov, A., Tweed, D., et al. 2013, *MNRAS*, 435, 999, doi: [10.1093/mnras/stt1338](https://doi.org/10.1093/mnras/stt1338)
- Dekel, A., Birnboim, Y., Engel, G., et al. 2009, *Nature*, 457, 451, doi: [10.1038/nature07648](https://doi.org/10.1038/nature07648)
- Di Matteo, T., Springel, V., & Hernquist, L. 2005, *Nature*, 433, 604, doi: [10.1038/nature03335](https://doi.org/10.1038/nature03335)
- Dolag, K., Borgani, S., Murante, G., & Springel, V. 2009, *MNRAS*, 399, 497, doi: [10.1111/j.1365-2966.2009.15034.x](https://doi.org/10.1111/j.1365-2966.2009.15034.x)
- Dome, T., Martin-Alvarez, S., Tacchella, S., Yuan, Y., & Sijacki, D. 2025, *MNRAS*, 537, 629, doi: [10.1093/mnras/staf006](https://doi.org/10.1093/mnras/staf006)
- Donnan, C. T., McLeod, D. J., Dunlop, J. S., et al. 2023, *MNRAS*, 518, 6011, doi: [10.1093/mnras/stac3472](https://doi.org/10.1093/mnras/stac3472)
- Donnan, C. T., McLure, R. J., Dunlop, J. S., et al. 2024, *MNRAS*, 533, 3222, doi: [10.1093/mnras/stae2037](https://doi.org/10.1093/mnras/stae2037)
- Draine, B. T. 2011, *Physics of the Interstellar and Intergalactic Medium*
- Dutton, A. A., van den Bosch, F. C., & Dekel, A. 2010, *MNRAS*, 405, 1690, doi: [10.1111/j.1365-2966.2010.16620.x](https://doi.org/10.1111/j.1365-2966.2010.16620.x)
- El-Badry, K., Wetzel, A., Geha, M., et al. 2016, *ApJ*, 820, 131, doi: [10.3847/0004-637X/820/2/131](https://doi.org/10.3847/0004-637X/820/2/131)
- Elbaz, D., Daddi, E., Le Borgne, D., et al. 2007, *A&A*, 468, 33, doi: [10.1051/0004-6361:20077525](https://doi.org/10.1051/0004-6361:20077525)
- Endsley, R., Chisholm, J., Stark, D. P., Topping, M. W., & Whitler, L. 2024a, *arXiv e-prints*, arXiv:2410.01905, doi: [10.48550/arXiv.2410.01905](https://doi.org/10.48550/arXiv.2410.01905)

- Endsley, R., Stark, D. P., Whitler, L., et al. 2024b, *MNRAS*, 533, 1111, doi: [10.1093/mnras/stae1857](https://doi.org/10.1093/mnras/stae1857)
- Faber, S. M., Willmer, C. N. A., Wolf, C., et al. 2007, *ApJ*, 665, 265, doi: [10.1086/519294](https://doi.org/10.1086/519294)
- Fabian, A. C. 2012, *ARA&A*, 50, 455, doi: [10.1146/annurev-astro-081811-125521](https://doi.org/10.1146/annurev-astro-081811-125521)
- Fardal, M. A., Katz, N., Gardner, J. P., et al. 2001, *ApJ*, 562, 605, doi: [10.1086/323519](https://doi.org/10.1086/323519)
- Faucher-Giguère, C.-A. 2018, *MNRAS*, 473, 3717, doi: [10.1093/mnras/stx2595](https://doi.org/10.1093/mnras/stx2595)
- Feldmann, R., Quataert, E., Hopkins, P. F., Faucher-Giguère, C.-A., & Kereš, D. 2017, *MNRAS*, 470, 1050, doi: [10.1093/mnras/stx1120](https://doi.org/10.1093/mnras/stx1120)
- Feldmann, R., Quataert, E., Faucher-Giguère, C.-A., et al. 2023, *MNRAS*, 522, 3831, doi: [10.1093/mnras/stad1205](https://doi.org/10.1093/mnras/stad1205)
- Forbes, J. C., Krumholz, M. R., Burkert, A., & Dekel, A. 2014, *MNRAS*, 438, 1552, doi: [10.1093/mnras/stt2294](https://doi.org/10.1093/mnras/stt2294)
- Fortuné, Silvio amnd Remus, R.-S., Kimmig, L. C., Burkert, A., & Dolag, K. 2025, arXiv e-prints, arXiv:2503.20858, doi: [10.48550/arXiv.2503.20858](https://doi.org/10.48550/arXiv.2503.20858)
- Harris, C. R., Millman, K. J., van der Walt, S. J., et al. 2020, *Nature*, 585, 357, doi: [10.1038/s41586-020-2649-2](https://doi.org/10.1038/s41586-020-2649-2)
- Hayward, C. C., & Hopkins, P. F. 2017, *MNRAS*, 465, 1682, doi: [10.1093/mnras/stw2888](https://doi.org/10.1093/mnras/stw2888)
- Hirschmann, M., Dolag, K., Saro, A., et al. 2014, *MNRAS*, 442, 2304, doi: [10.1093/mnras/stu1023](https://doi.org/10.1093/mnras/stu1023)
- Hogg, D. W., Blanton, M. R., Eisenstein, D. J., et al. 2003, *ApJL*, 585, L5, doi: [10.1086/374238](https://doi.org/10.1086/374238)
- Hopkins, P. F., Kereš, D., Oñorbe, J., et al. 2014a, *MNRAS*, 445, 581, doi: [10.1093/mnras/stu1738](https://doi.org/10.1093/mnras/stu1738)
- . 2014b, *MNRAS*, 445, 581, doi: [10.1093/mnras/stu1738](https://doi.org/10.1093/mnras/stu1738)
- Hopkins, P. F., Somerville, R. S., Hernquist, L., et al. 2006, *ApJ*, 652, 864, doi: [10.1086/508503](https://doi.org/10.1086/508503)
- Hopkins, P. F., Wetzel, A., Kereš, D., et al. 2018, *MNRAS*, 480, 800, doi: [10.1093/mnras/sty1690](https://doi.org/10.1093/mnras/sty1690)
- Hopkins, P. F., Wetzel, A., Wheeler, C., et al. 2023, *MNRAS*, 519, 3154, doi: [10.1093/mnras/stac3489](https://doi.org/10.1093/mnras/stac3489)
- Hunter, J. D. 2007, *Computing in Science & Engineering*, 9, 90, doi: [10.1109/MCSE.2007.55](https://doi.org/10.1109/MCSE.2007.55)
- Iyer, K. G., Tacchella, S., Genel, S., et al. 2020, *MNRAS*, 498, 430, doi: [10.1093/mnras/staa2150](https://doi.org/10.1093/mnras/staa2150)
- Katz, N., & Gunn, J. E. 1991, *ApJ*, 377, 365, doi: [10.1086/170367](https://doi.org/10.1086/170367)
- Kauffmann, G., Heckman, T. M., White, S. D. M., et al. 2003, *MNRAS*, 341, 54, doi: [10.1046/j.1365-8711.2003.06292.x](https://doi.org/10.1046/j.1365-8711.2003.06292.x)
- Kereš, D., Katz, N., Weinberg, D. H., & Davé, R. 2005, *MNRAS*, 363, 2, doi: [10.1111/j.1365-2966.2005.09451.x](https://doi.org/10.1111/j.1365-2966.2005.09451.x)
- Kravtsov, A., & Belokurov, V. 2024, arXiv e-prints, arXiv:2405.04578, doi: [10.48550/arXiv.2405.04578](https://doi.org/10.48550/arXiv.2405.04578)
- Leethochawalit, N., Trenti, M., Santini, P., et al. 2023, *ApJL*, 942, L26, doi: [10.3847/2041-8213/ac959b](https://doi.org/10.3847/2041-8213/ac959b)
- Leslie, S. K., Schinnerer, E., Liu, D., et al. 2020, *ApJ*, 899, 58, doi: [10.3847/1538-4357/aba044](https://doi.org/10.3847/1538-4357/aba044)
- Lilly, S. J., Carollo, C. M., Pipino, A., Renzini, A., & Peng, Y. 2013, *ApJ*, 772, 119, doi: [10.1088/0004-637X/772/2/119](https://doi.org/10.1088/0004-637X/772/2/119)
- Lu, S., Xu, D., Wang, S., et al. 2022, *MNRAS*, 509, 5062, doi: [10.1093/mnras/stab3228](https://doi.org/10.1093/mnras/stab3228)
- Lu, S., Xu, D., Wang, Y., et al. 2021, *MNRAS*, 503, 726, doi: [10.1093/mnras/stab497](https://doi.org/10.1093/mnras/stab497)
- Lyu, C., Wang, E., Zhang, H., et al. 2025, *ApJL*, 981, L6, doi: [10.3847/2041-8213/adb4ed](https://doi.org/10.3847/2041-8213/adb4ed)
- Madau, P., & Dickinson, M. 2014, *ARA&A*, 52, 415, doi: [10.1146/annurev-astro-081811-125615](https://doi.org/10.1146/annurev-astro-081811-125615)
- Mannucci, F., Cresci, G., Maiolino, R., Marconi, A., & Gnerucci, A. 2010, *MNRAS*, 408, 2115, doi: [10.1111/j.1365-2966.2010.17291.x](https://doi.org/10.1111/j.1365-2966.2010.17291.x)
- Marinacci, F., Vogelsberger, M., Pakmor, R., et al. 2018, *MNRAS*, 480, 5113, doi: [10.1093/mnras/sty2206](https://doi.org/10.1093/mnras/sty2206)
- Martizzi, D., Vogelsberger, M., Artale, M. C., et al. 2019, *MNRAS*, 486, 3766, doi: [10.1093/mnras/stz1106](https://doi.org/10.1093/mnras/stz1106)
- Mason, J. P., Patel, M. R., Pajola, M., et al. 2023, *Journal of Geophysical Research (Planets)*, 128, e2023JE008002, doi: [10.1029/2023JE008002](https://doi.org/10.1029/2023JE008002)
- Matthee, J., & Schaye, J. 2019, *MNRAS*, 484, 915, doi: [10.1093/mnras/stz030](https://doi.org/10.1093/mnras/stz030)
- McClymont, W., Tacchella, S., Smith, A., et al. 2025, arXiv e-prints, arXiv:2503.00106, doi: [10.48550/arXiv.2503.00106](https://doi.org/10.48550/arXiv.2503.00106)
- McQuinn, K. B. W., Skillman, E. D., Cannon, J. M., et al. 2010a, *ApJ*, 721, 297, doi: [10.1088/0004-637X/721/1/297](https://doi.org/10.1088/0004-637X/721/1/297)
- . 2010b, *ApJ*, 724, 49, doi: [10.1088/0004-637X/724/1/49](https://doi.org/10.1088/0004-637X/724/1/49)
- Mendez, A. J., Coil, A. L., Lotz, J., et al. 2011, *ApJ*, 736, 110, doi: [10.1088/0004-637X/736/2/110](https://doi.org/10.1088/0004-637X/736/2/110)
- Mihos, J. C., & Hernquist, L. 1996, *ApJ*, 464, 641, doi: [10.1086/177353](https://doi.org/10.1086/177353)
- Mintz, A., Setton, D. J., Greene, J. E., et al. 2025, arXiv e-prints, arXiv:2506.16510, doi: [10.48550/arXiv.2506.16510](https://doi.org/10.48550/arXiv.2506.16510)
- Morselli, L., Popesso, P., Erfanianfar, G., & Concas, A. 2017, *A&A*, 597, A97, doi: [10.1051/0004-6361/201629409](https://doi.org/10.1051/0004-6361/201629409)
- Muñoz López, C., Krajnović, D., Epinat, B., et al. 2025, arXiv e-prints, arXiv:2509.01710, doi: [10.48550/arXiv.2509.01710](https://doi.org/10.48550/arXiv.2509.01710)
- Murray, N., Quataert, E., & Thompson, T. A. 2005, *ApJ*, 618, 569, doi: [10.1086/426067](https://doi.org/10.1086/426067)
- Naiman, J. P., Pillepich, A., Springel, V., et al. 2018, *MNRAS*, 477, 1206, doi: [10.1093/mnras/sty618](https://doi.org/10.1093/mnras/sty618)

- Nelson, D., Pillepich, A., Springel, V., et al. 2018, *MNRAS*, 475, 624, doi: [10.1093/mnras/stx3040](https://doi.org/10.1093/mnras/stx3040)
- . 2019a, *MNRAS*, 490, 3234, doi: [10.1093/mnras/stz2306](https://doi.org/10.1093/mnras/stz2306)
- Nelson, D., Springel, V., Pillepich, A., et al. 2019b, *Computational Astrophysics and Cosmology*, 6, 2, doi: [10.1186/s40668-019-0028-x](https://doi.org/10.1186/s40668-019-0028-x)
- Noeske, K. G., Weiner, B. J., Faber, S. M., et al. 2007a, *ApJL*, 660, L43, doi: [10.1086/517926](https://doi.org/10.1086/517926)
- . 2007b, *ApJL*, 660, L43, doi: [10.1086/517926](https://doi.org/10.1086/517926)
- Orr, M. E., Hayward, C. C., Nelson, E. J., et al. 2017, *ApJL*, 849, L2, doi: [10.3847/2041-8213/aa8f93](https://doi.org/10.3847/2041-8213/aa8f93)
- Pannella, M., Elbaz, D., Daddi, E., et al. 2015, *ApJ*, 807, 141, doi: [10.1088/0004-637X/807/2/141](https://doi.org/10.1088/0004-637X/807/2/141)
- Pearson, W. J., Wang, L., Hurley, P. D., et al. 2018, *A&A*, 615, A146, doi: [10.1051/0004-6361/201832821](https://doi.org/10.1051/0004-6361/201832821)
- Peng, Y., Maiolino, R., & Cochrane, R. 2015, *Nature*, 521, 192, doi: [10.1038/nature14439](https://doi.org/10.1038/nature14439)
- Peng, Y.-j., Lilly, S. J., Kovač, K., et al. 2010, *ApJ*, 721, 193, doi: [10.1088/0004-637X/721/1/193](https://doi.org/10.1088/0004-637X/721/1/193)
- Pérez-González, P. G., Costantin, L., Langeroodi, D., et al. 2023, *ApJL*, 951, L1, doi: [10.3847/2041-8213/acd9d0](https://doi.org/10.3847/2041-8213/acd9d0)
- Perry, M. N., Taylor, A. J., Chavez Ortiz, O. A., et al. 2025, arXiv e-prints, arXiv:2510.05388, doi: [10.48550/arXiv.2510.05388](https://doi.org/10.48550/arXiv.2510.05388)
- Pillepich, A., Nelson, D., Hernquist, L., et al. 2018a, *MNRAS*, 475, 648, doi: [10.1093/mnras/stx3112](https://doi.org/10.1093/mnras/stx3112)
- Pillepich, A., Springel, V., Nelson, D., et al. 2018b, *MNRAS*, 473, 4077, doi: [10.1093/mnras/stx2656](https://doi.org/10.1093/mnras/stx2656)
- Pillepich, A., Nelson, D., Springel, V., et al. 2019, *MNRAS*, 490, 3196, doi: [10.1093/mnras/stz2338](https://doi.org/10.1093/mnras/stz2338)
- Planck Collaboration, Ade, P. A. R., Aghanim, N., et al. 2016, *A&A*, 594, A13, doi: [10.1051/0004-6361/201525830](https://doi.org/10.1051/0004-6361/201525830)
- Popesso, P., Concas, A., Cresci, G., et al. 2023, *MNRAS*, 519, 1526, doi: [10.1093/mnras/stac3214](https://doi.org/10.1093/mnras/stac3214)
- Renzini, A. 2016, *MNRAS*, 460, L45, doi: [10.1093/mnrasl/slw066](https://doi.org/10.1093/mnrasl/slw066)
- Robertson, B., Johnson, B. D., Tacchella, S., et al. 2024, *ApJ*, 970, 31, doi: [10.3847/1538-4357/ad463d](https://doi.org/10.3847/1538-4357/ad463d)
- Rodighiero, G., Daddi, E., Baronchelli, I., et al. 2011, *ApJL*, 739, L40, doi: [10.1088/2041-8205/739/2/L40](https://doi.org/10.1088/2041-8205/739/2/L40)
- Saintonge, A., & Catinella, B. 2022, *ARA&A*, 60, 319, doi: [10.1146/annurev-astro-021022-043545](https://doi.org/10.1146/annurev-astro-021022-043545)
- Salim, S. 2014, *Serbian Astronomical Journal*, 189, 1, doi: [10.2298/SAJ1489001S](https://doi.org/10.2298/SAJ1489001S)
- Salim, S., Rich, R. M., Charlot, S., et al. 2007, *ApJS*, 173, 267, doi: [10.1086/519218](https://doi.org/10.1086/519218)
- Schaye, J., Dalla Vecchia, C., Booth, C. M., et al. 2010, *MNRAS*, 402, 1536, doi: [10.1111/j.1365-2966.2009.16029.x](https://doi.org/10.1111/j.1365-2966.2009.16029.x)
- Schreiber, C., Pannella, M., Elbaz, D., et al. 2015, *A&A*, 575, A74, doi: [10.1051/0004-6361/201425017](https://doi.org/10.1051/0004-6361/201425017)
- Shen, X., Vogelsberger, M., Boylan-Kolchin, M., Tacchella, S., & Kannan, R. 2023, *MNRAS*, 525, 3254, doi: [10.1093/mnras/stad2508](https://doi.org/10.1093/mnras/stad2508)
- Shin, E.-j., Tacchella, S., Kim, J.-h., Iyer, K. G., & Semenov, V. A. 2023, *ApJ*, 947, 61, doi: [10.3847/1538-4357/acc251](https://doi.org/10.3847/1538-4357/acc251)
- Smethurst, R. J., Lintott, C. J., Simmons, B. D., et al. 2015, *MNRAS*, 450, 435, doi: [10.1093/mnras/stv161](https://doi.org/10.1093/mnras/stv161)
- Smith, D., Haberzettl, L., Porter, L. E., et al. 2022, *MNRAS*, 517, 4575, doi: [10.1093/mnras/stac2258](https://doi.org/10.1093/mnras/stac2258)
- Somerville, R. S., & Davé, R. 2015, *ARA&A*, 53, 51, doi: [10.1146/annurev-astro-082812-140951](https://doi.org/10.1146/annurev-astro-082812-140951)
- Sparre, M., Hayward, C. C., Feldmann, R., et al. 2017, *MNRAS*, 466, 88, doi: [10.1093/mnras/stw3011](https://doi.org/10.1093/mnras/stw3011)
- Speagle, J. S., Steinhardt, C. L., Capak, P. L., & Silverman, J. D. 2014a, *ApJS*, 214, 15, doi: [10.1088/0067-0049/214/2/15](https://doi.org/10.1088/0067-0049/214/2/15)
- . 2014b, *ApJS*, 214, 15, doi: [10.1088/0067-0049/214/2/15](https://doi.org/10.1088/0067-0049/214/2/15)
- Springel, V. 2010, *MNRAS*, 401, 791, doi: [10.1111/j.1365-2966.2009.15715.x](https://doi.org/10.1111/j.1365-2966.2009.15715.x)
- Springel, V., Di Matteo, T., & Hernquist, L. 2005, *MNRAS*, 361, 776, doi: [10.1111/j.1365-2966.2005.09238.x](https://doi.org/10.1111/j.1365-2966.2005.09238.x)
- Springel, V., & Hernquist, L. 2003, *MNRAS*, 339, 289, doi: [10.1046/j.1365-8711.2003.06206.x](https://doi.org/10.1046/j.1365-8711.2003.06206.x)
- Springel, V., White, S. D. M., Tormen, G., & Kauffmann, G. 2001, *MNRAS*, 328, 726, doi: [10.1046/j.1365-8711.2001.04912.x](https://doi.org/10.1046/j.1365-8711.2001.04912.x)
- Springel, V., Pakmor, R., Pillepich, A., et al. 2018, *MNRAS*, 475, 676, doi: [10.1093/mnras/stx3304](https://doi.org/10.1093/mnras/stx3304)
- Strateva, I., Ivezić, Ž., Knapp, G. R., et al. 2001, *AJ*, 122, 1861, doi: [10.1086/323301](https://doi.org/10.1086/323301)
- Sun, G., Faucher-Giguère, C.-A., Hayward, C. C., & Shen, X. 2023, *MNRAS*, 526, 2665, doi: [10.1093/mnras/stad2902](https://doi.org/10.1093/mnras/stad2902)
- Tacchella, S., Bose, S., Conroy, C., Eisenstein, D. J., & Johnson, B. D. 2018, *ApJ*, 868, 92, doi: [10.3847/1538-4357/aae8e0](https://doi.org/10.3847/1538-4357/aae8e0)
- Tacchella, S., Dekel, A., Carollo, C. M., et al. 2016, *MNRAS*, 457, 2790, doi: [10.1093/mnras/stw131](https://doi.org/10.1093/mnras/stw131)
- Tacchella, S., Forbes, J. C., & Caplar, N. 2020, *MNRAS*, 497, 698, doi: [10.1093/mnras/staa1838](https://doi.org/10.1093/mnras/staa1838)
- Tacchella, S., Trenti, M., & Carollo, C. M. 2013, *ApJL*, 768, L37, doi: [10.1088/2041-8205/768/2/L37](https://doi.org/10.1088/2041-8205/768/2/L37)
- Tacchella, S., Conroy, C., Faber, S. M., et al. 2022, *ApJ*, 926, 134, doi: [10.3847/1538-4357/ac449b](https://doi.org/10.3847/1538-4357/ac449b)
- Tolstoy, E., Hill, V., & Tosi, M. 2009, *ARA&A*, 47, 371, doi: [10.1146/annurev-astro-082708-101650](https://doi.org/10.1146/annurev-astro-082708-101650)

- Torrey, P., Vogelsberger, M., Marinacci, F., et al. 2019, MNRAS, 484, 5587, doi: [10.1093/mnras/stz243](https://doi.org/10.1093/mnras/stz243)
- Tully, R. B., Mould, J. R., & Aaronson, M. 1982, ApJ, 257, 527, doi: [10.1086/160009](https://doi.org/10.1086/160009)
- van Loon, M. L., Mitchell, P. D., & Schaye, J. 2021, MNRAS, 504, 4817, doi: [10.1093/mnras/stab1254](https://doi.org/10.1093/mnras/stab1254)
- Virtanen, P., Gommers, R., Oliphant, T. E., et al. 2020, Nature Methods, 17, 261, doi: [10.1038/s41592-019-0686-2](https://doi.org/10.1038/s41592-019-0686-2)
- Vogelsberger, M., Sijacki, D., Kereš, D., Springel, V., & Hernquist, L. 2012, MNRAS, 425, 3024, doi: [10.1111/j.1365-2966.2012.21590.x](https://doi.org/10.1111/j.1365-2966.2012.21590.x)
- Wan, J. T., Tacchella, S., D'Eugenio, F., Johnson, B. D., & van der Wel, A. 2025, MNRAS, 539, 2891, doi: [10.1093/mnras/staf657](https://doi.org/10.1093/mnras/staf657)
- Wan, J. T., Tacchella, S., Johnson, B. D., et al. 2024, MNRAS, 532, 4002, doi: [10.1093/mnras/stae1734](https://doi.org/10.1093/mnras/stae1734)
- Wang, B., Cappellari, M., Peng, Y., & Graham, M. 2020, MNRAS, 495, 1958, doi: [10.1093/mnras/staa1325](https://doi.org/10.1093/mnras/staa1325)
- Wang, B., Peng, Y., & Cappellari, M. 2025, Nature Astronomy, 9, 165, doi: [10.1038/s41550-024-02376-8](https://doi.org/10.1038/s41550-024-02376-8)
- Wang, E., Kong, X., & Pan, Z. 2018, ApJ, 865, 49, doi: [10.3847/1538-4357/aadb9e](https://doi.org/10.3847/1538-4357/aadb9e)
- Wang, E., & Lilly, S. J. 2020, ApJ, 892, 87, doi: [10.3847/1538-4357/ab7b7d](https://doi.org/10.3847/1538-4357/ab7b7d)
- . 2021, ApJ, 910, 137, doi: [10.3847/1538-4357/abe413](https://doi.org/10.3847/1538-4357/abe413)
- . 2022a, ApJ, 927, 217, doi: [10.3847/1538-4357/ac49ed](https://doi.org/10.3847/1538-4357/ac49ed)
- . 2022b, ApJ, 929, 95, doi: [10.3847/1538-4357/ac5e31](https://doi.org/10.3847/1538-4357/ac5e31)
- . 2023a, ApJ, 944, 143, doi: [10.3847/1538-4357/acaf31](https://doi.org/10.3847/1538-4357/acaf31)
- . 2023b, ApJ, 955, 55, doi: [10.3847/1538-4357/acecfd](https://doi.org/10.3847/1538-4357/acecfd)
- Wang, E., Lilly, S. J., Pezzulli, G., & Matthee, J. 2019, ApJ, 877, 132, doi: [10.3847/1538-4357/ab1c5b](https://doi.org/10.3847/1538-4357/ab1c5b)
- Wang, S., Xu, D., Lu, S., et al. 2022, MNRAS, 509, 3148, doi: [10.1093/mnras/stab3167](https://doi.org/10.1093/mnras/stab3167)
- Weisz, D. R., Dalcanton, J. J., Williams, B. F., et al. 2011, ApJ, 739, 5, doi: [10.1088/0004-637X/739/1/5](https://doi.org/10.1088/0004-637X/739/1/5)
- Whitaker, K. E., van Dokkum, P. G., Brammer, G., & Franx, M. 2012a, ApJL, 754, L29, doi: [10.1088/2041-8205/754/2/L29](https://doi.org/10.1088/2041-8205/754/2/L29)
- . 2012b, ApJL, 754, L29, doi: [10.1088/2041-8205/754/2/L29](https://doi.org/10.1088/2041-8205/754/2/L29)
- White, S. D. M., & Rees, M. J. 1978, MNRAS, 183, 341, doi: [10.1093/mnras/183.3.341](https://doi.org/10.1093/mnras/183.3.341)
- Whitler, L., Stark, D. P., Topping, M. W., et al. 2025, arXiv e-prints, arXiv:2501.00984, doi: [10.48550/arXiv.2501.00984](https://doi.org/10.48550/arXiv.2501.00984)
- Wuyts, S., Förster Schreiber, N. M., van der Wel, A., et al. 2011, ApJ, 742, 96, doi: [10.1088/0004-637X/742/2/96](https://doi.org/10.1088/0004-637X/742/2/96)
- Yin, J., Shen, S., & Hao, L. 2023, ApJ, 958, 34, doi: [10.3847/1538-4357/acfa6b](https://doi.org/10.3847/1538-4357/acfa6b)
- Zhang, J., Wuyts, S., Cutler, S. E., et al. 2023, MNRAS, 524, 4128, doi: [10.1093/mnras/stad2066](https://doi.org/10.1093/mnras/stad2066)
- Zolotov, A., Dekel, A., Mandelker, N., et al. 2015, MNRAS, 450, 2327, doi: [10.1093/mnras/stv740](https://doi.org/10.1093/mnras/stv740)